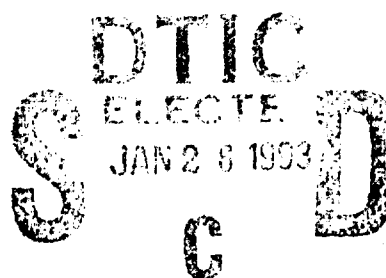


AD-A259 726



Quarterly Technical Report

Solid State Research



1992:2

Lincoln Laboratory
MASSACHUSETTS INSTITUTE OF TECHNOLOGY
LEXINGTON, MASSACHUSETTS

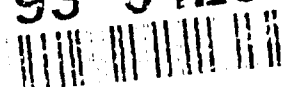


Prepared for the Department of the Air Force under Contract F19628-90-C-0002.

Approved for public release; distribution is unlimited.

**BEST
AVAILABLE COPY**

93-01264



93 1 25 012

This report is based on studies performed at Lincoln Laboratory, a center for research operated by Massachusetts Institute of Technology. The work was sponsored by the Strategic Defense Initiative Organization under Air Force Contract F19628-90-C-0002.

This report may be reproduced to satisfy needs of U.S. Government agencies.

The ESD Public Affairs Office has reviewed this report, and it is releasable to the National Technical Information Service, where it will be available to the general public, including foreign nationals.

This technical report has been reviewed and is approved for publication.

FOR THE COMMANDER


Gary T. Tungian
Administrative Contracting Officer
Directorate of Contracted Support Management

Non-Lincoln Recipients

PLEASE DO NOT RETURN

Permission is given to destroy this document
when it is no longer needed.

MASSACHUSETTS INSTITUTE OF TECHNOLOGY
LINCOLN LABORATORY

SOLID STATE RESEARCH

QUARTERLY TECHNICAL REPORT

1 FEBRUARY — 30 APRIL 1992

ISSUED 21 SEPTEMBER 1992

Approved for public release; distribution is unlimited.

Accession For	
NTIS Grant	<input checked="" type="checkbox"/>
DTIC TAB	<input type="checkbox"/>
Unannounced	<input type="checkbox"/>
Justification	
By	
Distribution/	
As a result of	
and/or	
From	
A-1	

LEXINGTON

MASSACHUSETTS

ABSTRACT

This report covers in detail the research work of the Solid State Division at Lincoln Laboratory for the period 1 February through 30 April 1992. The topics covered are Electrooptical Devices, Quantum Electronics, Materials Research, Submicrometer Technology, High Speed Electronics, Microelectronics, and Analog Device Technology. Funding is provided primarily by the Air Force, with additional support provided by the Army, DARPA, Navy, SDIO, NASA, and DOE.

TABLE OF CONTENTS

Abstract	iii
List of Illustrations	vii
List of Tables	x
Introduction	xi
Reports on Solid State Research	xiii
Organization	xxiii
 1. ELECTROOPTICAL DEVICES	 1
1.1 External-Modulator Analog Link with Optical Amplifier	1
1.2 Large-Numerical-Aperture Microlenses Fabricated by One-Step Ion-Beam Etching and Mass-Transport Smoothing	3
1.3 GaInAsP Strained Layers for GaAs-Based Diode Lasers	6
1.4 Ridge Waveguide Lasers for High-Speed Free-Space Optical Interconnections	9
 2. QUANTUM ELECTRONICS	 15
2.1 Diode-Pumped Microchip Lasers Electrooptically <i>Q</i> Switched at High Pulse Repetition Rates	15
2.2 High-Power, Continuous-Wave Microchip Laser Array	17
2.3 Frequency-Modulated Microwave Source Using Beats between Orthogonal Modes of a Single Laser	20
 3. MATERIALS RESEARCH	 25
3.1 Measurement of RHEED Oscillations during MBE Growth of GaAs on a Rotating Substrate	25
3.2 Time and Temperature Dependence of Phosphorus Vapor Pressure	29
 4. SUBMICROMETER TECHNOLOGY	 35
4.1 Laser-Induced Damage in Pellicles at 193 nm	35
4.2 Ionic Liquid-Channel Field-Effect Transistor	38
 5. HIGH SPEED ELECTRONICS	 43
5.1 Definitive Identification of D^- Centers in GaAs Quantum Wells by Tilt-Induced Line Splitting in a Magnetic Field	43

TABLE OF CONTENTS (Continued)

6.	MICROELECTRONICS	47
6.1	DNA Sequence Detection Using Charge-Coupled Devices	47
7.	ANALOG DEVICE TECHNOLOGY	51
7.1	Multilayer 12-GHz Microstrip Antenna Array with a High- T_c Superconducting Feed Network	51

LIST OF ILLUSTRATIONS

Figure No.		Page
1-1	Schematic layout of external-modulator analog link with optical amplifier.	1
1-2	Plot of link SNR vs optical transmission T . For the link with an amplifier, T is the transmission between the amplifier output and the receiver. For the link without an amplifier, T represents the transmission between the modulator output and the receiver.	2
1-3	Present technique of microlens fabrication by one-step ion-beam etching and mass-transport smoothing.	3
1-4	Scanning electron micrograph perspective views of (a) a mesa structure produced by ion-beam-assisted etching and (b) a microlens formed after mass-transport smoothing.	4
1-5	Stylus surface profile of the fabricated microlens (solid curve) compared with a calculated spherical profile (dots).	5
1-6	Optical micrographs of (a) an etched mesa structure, (b) a microlens formed after mass transport, and (c) an image formed by the microlens surface. The vertical striations in (b) are the partially focused image of the tungsten filament in the microscope light source.	5
1-7	Undoped separate-confinement heterostructure with strained GaInAsP quantum well.	7
1-8	Rocking curve of eight-period structure with $\text{Ga}_x\text{In}_{1-x}\text{As}_y\text{P}_{1-y}$ strained layer and 590-nm GaAs spacer layer. The lower curve, shifted downward by an order of magnitude for visualization purposes, is a simulated rocking curve for $x = 0.60$ and $y = 0.44$, a 9.8-nm strained-layer thickness, and a 59-nm GaAs thickness. The reflection is (004) with Cu K_α radiation, and the diffraction angle origin is taken at the Bragg angle for GaAs.	8
1-9	Room-temperature photoluminescence from the structure of Figure 1-7. Excitation is at 514 nm, and a photomultiplier with S-1 response is used for detection.	9
1-10	Cross-sectional schematic diagram of InGaAs/AlGaAs ridge waveguide laser structure showing the double-quantum-well active region.	10
1-11	Plots of (a) pulsed threshold current and (b) differential quantum efficiency, both as a function of nominal ridge width for two 500- μm -long, uncoated ridge waveguide laser bars.	11

LIST OF ILLUSTRATIONS (Continued)

Figure No.		Page
1-12	Plots of (a) average pulsed threshold current and (b) average differential quantum efficiency, both as a function of nominal ridge width for 200-, 250-, 350-, and 500- μm -long, uncoated ridge waveguide laser bars. The data for the 500- μm -long laser bar represent an average of all devices from the better bar (1) in Figure 1-11.	12
1-13	Output power per facet vs pulse input current for a 2.5- μm -wide, 200- μm -long uncoated ridge waveguide laser.	13
2-1	Full width at half-maximum of the output pulses obtained from a 1.064- μm , diode-pumped, electrooptically Q -switched Nd:YAG microchip laser as a function of pulse repetition rate.	16
2-2	Schematic diagram of the experimental setup. The Nd:YAG microchip slab is bonded to the sapphire heatsink, which in turn is heatsunk by the water-cooled copper collar at the output end. This arrangement minimizes transverse thermal gradients and edge effects in the Nd:YAG slab.	18
2-3	Output power from the Nd:YAG laser array as a function of incident pump power. Diode laser temperature is varied to maximize Nd:YAG laser output.	19
2-4	(a) Schematic of the laser-generated frequency-modulated microwave source. A single Nd:YAG laser is operated simultaneously in two polarizations. To generate microwaves, the output is passed through a polarizer oriented at 45° so that the difference frequency can be generated in a fast photomixer. (b) Fabry-Perot spectra of the laser output in vertical and horizontal polarizations. The top two spectra show that the laser has predominantly one vertically polarized mode but with two other weaker modes also apparent; the frequency shifts at $\sim 5 \text{ MHz/V}$. The bottom spectrum shows that the laser operates in only one mode of horizontal polarization; the frequency does not change with applied voltage.	21
2-5	Tuning of the microwave frequency. The microwave signal tuned with voltage with a sensitivity of 4.4 MHz/V.	22
2-6	Microwave spectrum of the photomixer. The microwave intensity is -54 dBm and is limited by the amount of optical power that can be dissipated in the photomixer. The relaxation oscillation sidebands that are 320 kHz from the main peak are suppressed by 40 dB from the principal microwave beat note.	22
3-1	Schematic of video tracking and data analysis system.	26
3-2	Power spectrum of RHEED intensity data for a nonrotating GaAs sample.	27

LIST OF ILLUSTRATIONS (Continued)

Figure No.		Page
3-3	RHEED intensity data for the same sample as in Figure 3-2 taken at a rotation rate of 5 rpm.	28
3-4	Power spectrum of data from Figure 3-3.	28
3-5	Schematic diagram of apparatus for measuring phosphorus pressure.	29
3-6	Phosphorus pressures measured during heating and cooling vs reciprocal absolute temperature.	30
3-7	Phosphorus pressure vs time at constant temperature.	31
4-1	Change in thickness of a DuPont and an Exion pellicle, exposed at 193 nm at a fluence of $5 \text{ mJ cm}^{-2}/\text{pulse}$.	36
4-2	Logarithmic plot of the number of 193-nm pulses required to rupture a pellicle, for several fluences in the range 4 to $100 \text{ mJ cm}^{-2}/\text{pulse}$. The pellicles tested were from DuPont (initial thickness $0.83 \text{ }\mu\text{m}$) and Exion (initial thicknesses 1.18 and $3.26 \text{ }\mu\text{m}$). At the fluences expected at the mask in a stepper ($\sim 0.1 \text{ mJ cm}^{-2}/\text{pulse}$), the pellicles would rupture in 10^{10} – 10^{11} pulses.	37
4-3	Evolution of the thickness of Teflon AF 1600 thin films on fused silica (normalized to their initial thickness) with increasing number of 193-nm pulses, for the four fluences indicated.	38
4-4	(a) Transverse and (b) longitudinal cross sections of the ILCFET (not to scale).	39
4-5	Scanning electron micrograph of two parallel open-air channels just after an etch of sacrificial amorphous Si. The openings to the channels are the dark areas.	40
4-6	Theoretical steady-state and non-steady-state channel conductance vs gate voltage curves for a channel filled with $5 \times 10^{-4}\text{-M}$ acid in glycerol with cation and anion mobility of 7.85×10^{-6} and $1 \times 10^{-6} \text{ cm}^2 \text{ V}^{-1} \text{ s}^{-1}$, respectively. The non-steady-state curve is interpolated from 10-V steps in gate voltage, starting at 20 V and occurring 66.7 min apart, in which the gate capacitance is fully charged but the device has not reached steady state by ambipolar diffusion before the gate voltage is stepped again.	41
4-7	Experimental non-steady-state channel conductance vs gate voltage curve for a $1.8 \times 10^{-3}\text{-M}$ glycerol solution of H_3BO_3 . The hysteresis is counterclockwise, as predicted in Figure 4-6.	41

LIST OF ILLUSTRATIONS (Continued)

Figure No.		Page
5-1	Photoconductivity data above (84.94 cm^{-1}) and below (54.26 cm^{-1}) the D^- level crossing for $\theta = 0^\circ$ and 31° . Vertical lines (dashed for $\theta = 31^\circ$ and solid for $\theta = 0^\circ$) locate the D^- peaks. The strong lower-field peaks are from the donor $1s \rightarrow 2p_{+1}$ transition.	44
5-2	Transition energy vs magnetic field for line b of [4]. The magnetic field in (a) to (c) makes an angle $\theta = 0^\circ$, 16° , and 31° , respectively, relative to the normal to the well planes. The dots represent data and the solid lines represent theory. The diamond is a data point for $\theta = 26^\circ$. The dashed lines in (b) and (c) display the theoretical results for $\theta = 0^\circ$.	45
6-1	Implementation of sequencing by hybridization using a 420×420 imager, showing arrays of DNA probes (a) before and (b) after hybridization.	48
6-2	Hybridization map generated by a CCD imager.	49
7-1	(a) Cross section of a single stacked patch in a superconductive microstrip antenna array. (b) Diagram of the structure of the superconductive microstrip stacked-patch antenna array.	51
7-2	Input reflection coefficient vs frequency for superconducting YBCO elements in a cryogenic infinite-array waveguide simulator. Bandwidth is measured using a 2:1 VSWR criterion.	52
7-3	Silver upper radiator array (left) and YBCO lower feed array (right) of disassembled superconducting microstrip antenna array.	53
7-4	Far-field radiation patterns of the superconducting YBCO microstrip array at 12 GHz. Both E - and H -plane patterns were sufficiently symmetric that only half of each is shown on the left- and right-hand sides of the figure, respectively.	53

LIST OF TABLES

Table No.		Page
2-1	Characteristics of the Output Pulses from a $1.064\text{-}\mu\text{m}$, Diode-Pumped, Electrooptically Q -Switched Nd:YAG Microchip Laser	17
6-1	Example of Sequencing by Hybridization	47

INTRODUCTION

1. ELECTROOPTICAL DEVICES

An external-modulator analog link has been demonstrated that uses a high-gain Er-doped fiber amplifier. High signal-to-noise ratio is maintained over more than a 20-dB range of optical attenuation between the amplifier and receiver.

Large-numerical-aperture microlenses have been fabricated by one-step ion-beam-assisted etching and mass transport. This new, relatively simple technique is potentially superior to the conventional ones.

Strained-layer GaInAsP quantum-well structures, suitable for laser emission at 830 nm, have been grown by organometallic vapor phase epitaxy. X-ray and photoluminescence studies indicate that these are of very high quality and are comparable to previously reported structures with InGaAs quantum wells, which were developed for laser emission at 980 nm.

The effect of ridge width and laser length on both threshold current I_{th} and differential quantum efficiency η_d of InGaAs/AlGaAs quantum-well, ridge waveguide diode lasers has been investigated. For lasers with 500- μ m-long cavities, I_{th} was typically in the range 6–7 mA and η_d was > 40% per facet for 2–3- μ m-wide ridges, whereas an uncoated 2.5- μ m-wide, 200- μ m-long device had an I_{th} of 4.5 mA and an η_d of 44% per facet.

2. QUANTUM ELECTRONICS

A transversely extended, flat-flat monolithic Nd:YAG laser cavity has been pumped by a two-dimensional diode laser array to form an array of CW microchip laser emitters with a total output power of 9.8 W for a pump power of 38.5 W. The ensemble slope efficiency was 32%, the overall optical efficiency was 25%, and the beams were shown to have excellent spatial-mode quality and parallelism.

Approximately 50 mW of time-averaged 1.064- μ m output power has been obtained from a diode-pumped, electrooptically Q-switched Nd:YAG microchip laser at pulse repetition rates between 5 and 500 kHz. The full width at half-maximum of the output pulses is proportional to the repetition rate, varying from < 300 ps at low repetition rates to 15 ns at 500 kHz.

A single laser has been operated simultaneously in two orthogonally polarized modes, which allows microwave beat generation with more stability than can be obtained with two separate free-running lasers. The design allows electrooptic tuning of one of the laser modes and a tuning sensitivity of 4.5 MHz/V.

3. MATERIALS RESEARCH

By combining a computerized video tracking system with a procedure reported earlier for frequency-domain analysis, a technique has been devised for the measurement and analysis of reflection high-energy electron diffraction (RHEED) oscillations occurring during molecular beam epitaxy on a rotating substrate. Previously, it has been necessary to stop substrate rotation in order to perform RHEED oscillation analysis.

The phosphorus vapor pressure in sealed fused silica ampoules has been measured as a function of time and temperature by utilizing the apparatus and technique developed earlier for pressure-balanced synthesis of InP. It was found that because of kinetic limitations on phosphorus sublimation, condensation, and condensed-phase transformation, the phosphorus pressure during InP synthesis is not in general equal to the equilibrium vapor pressure of amorphous red phosphorus at the reservoir temperature.

4. SUBMICROMETER TECHNOLOGY

Measurements have been made to determine the damaging effects of 193-nm excimer laser radiation on pellicles designed for use in 248-nm lithography systems. Prolonged irradiation causes gradual thinning and eventual rupture of the pellicle, but our results indicate that these effects will be minimal for several years' operation in a full-production environment.

An ionic liquid-channel field-effect transistor has been designed, fabricated, and tested. In this new device, which functions as a monolithic chemical analyzer, current is carried in thin channels by ions of liquid electrolyte.

5. HIGH SPEED ELECTRONICS

D^- centers have been unambiguously identified in GaAs/AlGaAs quantum wells by analysis of the dependence of the observed photoconductivity spectrum on the applied magnetic field and sample orientation. Excellent agreement between theory and experiment was obtained without any adjustable parameters.

6. MICROELECTRONICS

A charge-coupled device (CCD) has been used to detect hybridization of target DNA to probe DNA. The CCD detected beta particle emission from the radioisotope label ^{32}P that is present at hybridized sites.

7. ANALOG DEVICE TECHNOLOGY

A multilayer microstrip antenna array has been fabricated with a high- T_c superconducting feed network as the lower layer in the structure. The superconductive array operated at 12 GHz with an 8% bandwidth and a gain of 15 dBi.

REPORTS ON SOLID STATE RESEARCH

1 FEBRUARY THROUGH 30 APRIL 1992

PUBLICATIONS

- | | | |
|--|--|--|
| Optimization of Externally Modulated Analog Optical Links | G. E. Betts
L. M. Johnson
C. H. Cox III | <i>Proc. SPIE</i> 1562 , 281 (1991) |
| Nonlinear Electrodynamics of Superconducting NbN and Nb Thin Films at Microwave Frequencies | C. C. Chin*
D. E. Oates
G. Dresselhaus*
M. S. Dresselhaus* | <i>Phys. Rev. B</i> 45 , 4788 (1992) |
| Real-Time Characterization of Acoustic Modes of Polyimide Thin-Film Coatings Using Impulsive Stimulated Thermal Scattering | A. R. Duggal*
J. A. Rogers*
K. A. Nelson*
M. Rothschild | <i>Appl. Phys. Lett.</i> 60 , 692 (1992) |
| MBE Growth, Material Properties, and Performance of GaSb-Based 2.2 μm Diode Lasers | S. J. Eglash
H. K. Choi | <i>In Gallium Arsenide and Related Compounds 1991</i> ,
G. B. Stringfellow, ed.
(IOP Publishing, Bristol, England, 1992), p. 487 |
| Spatial Modes of a Concentric-Circle-Grating Surface-Emitting, AlGaAs/GaAs Quantum Well Semiconductor Laser | T. Erdogan*
O. King*
G. W. Wicks*
D. G. Hall*
C. L. Dennis
M. J. Rooks* | <i>Appl. Phys. Lett.</i> 60 , 1773 (1992) |
| High-Speed Experiments on a QFP-Based Comparator for ADC's with 18-GHz Sample Rate and 5-GHz Input Frequency | Y. Harada*
J. B. Green | <i>IEEE Trans. Appl. Superconduct.</i> 2 , 21 (1992) |

*Author not at Lincoln Laboratory.

- | | | |
|---|---|---|
| Silylation of Focused Ion Beam Exposed Resists | M. A. Hartney
D. C. Shaver
M. I. Shepard*
J. S. Huh*
J. Melngailis | <i>Appl. Phys. Lett.</i> 59 , 485 (1991) |
| Vapor Etching of GaAs and AlGaAs by CH ₃ I | C. W. Krueger
C. A. Wang
M. Flytzani-Stephanopoulos* | <i>Appl. Phys. Lett.</i> 60 , 1459 (1992) |
| High-Brightness Diode-Laser-Pumped Semiconductor Heterostructure Lasers | H. Q. Le
W. D. Goodhue
S. Di Cecca | <i>Appl. Phys. Lett.</i> 60 , 1280 (1992) |
| Reactions of Hydrogenated Defects in Fused Silica Caused by Thermal Treatment and Deep Ultraviolet Irradiation | D. H. Levy*
K. K. Gleason*
M. Rothschild
J. H. C. Sedlacek
R. Takke* | <i>Appl. Phys. Lett.</i> 60 , 1667 (1992) |
| Microchannel Heat Sinks with High Uniformity of Temperature | L. J. Missaggia
J. N. Walpole | <i>Proc. SPIE</i> 1582 , 106 (1991) |
| Definitive Identification of D^- Centers in GaAs Quantum Wells by Tilt-Induced Line Splitting in a Magnetic Field | E. R. Mueller*
D. M. Larsen*
J. Waldman*
W. D. Goodhue | <i>Phys. Rev. Lett.</i> 68 , 2204 (1992) |
| High Frequency Oscillators Based on Resonant Tunneling | T. C. L. G. Sollner
E. R. Brown
J. R. Söderström*
T. C. McGill*
C. D. Parker
W. D. Goodhue | <i>In Resonant Tunneling in Semiconductors: Physics and Applications</i> , L. L. Chang, E. E. Mendez, and C. Tejedor, eds. (Plenum, New York, 1991), p. 487 |
| Free-Space Board-to-Board Optical Interconnections | D. Z. Tsang | <i>Proc. SPIE</i> 1563 , 66 (1991) |
| New Materials for Diode Laser Pumping of Solid-State Lasers | C. A. Wang
S. H. Groves | <i>IEEE J. Quantum Electron.</i> 28 , 942 (1992) |

*Author not at Lincoln Laboratory.

- | | | |
|--|--|--|
| OMVPE Regrowth of CH ₃ I-Vapor-Etched GaAs | C. A. Wang
C. W. Krueger
M. Flytzani-Stephanopoulos*
R. A. Brown* | <i>J. Electron. Mater.</i> 21 , 299 (1992) |
| Substrate Temperature Measurements Using Ultrasonically Bonded Platinum II Thermocouples | A. C. Westerheim
A. C. Anderson
M. J. Cima* | <i>Rev. Sci. Instrum.</i> 63 , 2282 (1992) |
| Frequency Tuning of Microchip Lasers Using Pump-Power Modulation | J. J. Zayhowski
J. A. Keszenheimer | <i>IEEE J. Quantum Electron.</i> 28 , 1118 (1992) |

ACCEPTED FOR PUBLICATION

- | | | |
|---|--|-------------------------------------|
| Flow Regime Map and Desorption Rate Uniformity in Vertical Rotating-Disk OMVPE Reactors | C. R. Biber*
C. A. Wang
S. Motakef* | <i>J. Cryst. Growth</i> |
| Stereo Laser Micromachining of Silicon | T. Bloomstein
D. J. Ehrlich | <i>Appl. Phys. Lett.</i> |
| Analytic Model of Shot Noise in Double-Barrier Resonant-Tunneling Diodes | E. R. Brown | <i>IEEE Trans. Electron Devices</i> |
| Sub-0.25- μ m Resolution Using 193-nm Optical Lithography | M. A. Hartney
M. W. Horn
R. R. Kunz
M. Rothschild
D. C. Shaver | <i>Microlithogr. World</i> |
| Phase Locking of 1.32- μ m Microchip Lasers Using Pump-Diode Modulation | J. A. Keszenheimer
J. J. Zayhowski
E. J. Balboni* | <i>Opt. Lett.</i> |

*Author not at Lincoln Laboratory.

Broadband Traveling-Wave Directional-Coupler Electrooptic Modulator in AlGaAs/GaAs	M. N. Khan* A. Gopinath* J. P. G. Bristow* J. P. Donnelly	<i>IEEE Trans. Microwave Theory Tech.</i>
Modeling the Nonlinearity of Superconducting Strip Transmission Lines	C. W. Lam* D. M. Sheen* S. M. Ali* D. E. Oates	<i>IEEE Trans. Appl. Superconduct.</i>
Full Wave Characterization of High- T_c Superconducting Transmission Lines	L. H. Lee* S. M. Ali* W. G. Lyons	<i>IEEE Trans. Appl. Superconduct.</i>
Microchannel Heat Sinks for Two-Dimensional Diode Laser Arrays	J. N. Walpole L. J. Missaggia	<i>In Surface Emitting Semiconductor Lasers and Arrays</i> , J. M. Hammer and G. A. Evans, eds. (Academic, Orlando, Fla.)
Horizontal Cavity Surface Emitting Lasers with Integrated Beam Deflectors	R. C. Williamson J. P. Donnelly Z. L. Liao W. D. Goodhue J. N. Walpole	<i>In Surface Emitting Semiconductor Lasers and Arrays</i> , J. M. Hammer and G. A. Evans, eds. (Academic, Orlando, Fla.)

PRESENTATIONS[†]

Vertical Gradient-Freeze Growth of $\text{SrAl}_{0.5}\text{Ta}_{0.5}\text{O}_3$ and $\text{SrAl}_{0.5}\text{Nb}_{0.5}\text{O}_3$	A. J. Strauss R. E. Fahey	Workshop on Substrate Materials, Williamsburg, Virginia, 5-7 February 1992
Modeling of Energy Storage Yb:YAG Lasers and Amplifiers	T. Y. Fan P. Lacovara	} Advanced Solid-State Lasers Meeting, Santa Fe, New Mexico, 17-19 February 1992
Energy Transfer and Upconversion in Yb:Er:YAG	P. Lacovara	

*Author not at Lincoln Laboratory.

[†]Titles of presentations are listed for information only. No copies are available for distribution.

High-Power Nd:YAG Microchip
Laser Arrays

C. D. Nabors
J. J. Zayhowski
R. L. Aggarwal
J. R. Ochoa
J. L. Daneu
A. Mooradian

Advanced Solid-State Lasers
Meeting,
Santa Fe, New Mexico,
17-19 February 1992

Application and Performance
Characterization of Schottky-Barrier
and GeSi-Heterojunction Sensors

M. J. Cantella
M. H. Ide
P. J. O'Donnell
P. J. Shread
P. D. Tennyson
B-Y. Tsaur

IRIS Specialty Group on
Passive Sensors,
Laurel, Maryland,
18-20 February 1992

MWIR-LWIR Multispectral $\text{Ge}_x\text{Si}_{1-x}/\text{Si}$
Heterojunction Focal Plane Arrays

B-Y. Tsaur
C. K. Chen
S. A. Marino

Resonant-Tunneling-Diode Speed
Limits and Applications in Fast
Logic Circuits

E. R. Brown
M. A. Hollis
F. W. Smith

1992 IEEE International Solid-
State Circuits Conference,
San Francisco, California,
19-21 February 1992

Recent Developments in Strained
Quantum-Well Diode Lasers

H. K. Choi

Korean Scientists and
Engineers Association Regional
Conference,
Cambridge, Massachusetts,
6-7 March 1992

Modeling and Optimization of
Silylation Processes for 193-nm
Lithography

M. A. Hartney

Silylation Process for 193-nm
Lithography Using Acid Catalyzed
Resists

M. A. Hartney
J. W. Thackeray*

1992 Symposium on
Microlithography,
San Jose, California,
8-13 March 1992

*Author not at Lincoln Laboratory.

A Comparison of Etching Tools
for Resist Pattern Transfer

M. W. Horn
M. A. Hartney
R. R. Kunz

Surface-Imaged Silicon Polymers for
193-nm Excimer Laser Lithography

R. R. Kunz
M. W. Horn
R. B. Goodman
G. M. Wallraff*
R. D. Miller*
P. A. Bianconi*

1992 Symposium on
Microlithography,
San Jose, California,
8-13 March 1992

Laser Induced Damage in Pellicles
at 193 nm

M. Rothschild
J. H. C. Sedlacek

A Small-Field Stepper for 193-nm
Lithography Process Development

D. C. Shaver
D. M. Craig
C. A. Marchi
M. A. Hartney
F. Goodall*

Optical Lithography at Feature Sizes
of 0.25 μm and Below

M. A. Hartney
M. W. Horn
R. R. Kunz
M. Rothschild
D. C. Shaver

Technical Seminar, Intel,
Santa Clara, California,
11 March 1992

Nonlinear Electrodynamics of
Superconducting YBCO Thin Films
at Microwave Frequencies

P. Nguyen*
D. E. Oates
C. C. Chin*
G. Dresselhaus*
M. Dresselhaus*

March Meeting of the
American Physical Society,
Indianapolis, Indiana,
16-20 March 1992

Microwave Measurements of
Superconducting Films in the
Mixed State

J. Steinbeck*
D. E. Oates
A. C. Anderson
N. Newman*

*Author not at Lincoln Laboratory.

**Free-Space Optical Interconnections
for Parallel Computers**

**D. Z. Tsang
T. J. Goblick**

**Packaging, Interconnects and
Optoelectronics for the Design of
Parallel Computers Workshop,
Schaumburg, Illinois,
18-19 March 1992**

Integrated Optics

L. M. Johnson

**Lincoln Laboratory
Technical Seminar Series,
Carnegie-Mellon University,
Pittsburgh, Pennsylvania,
19 March 1992**

**Device Applications and Characterization
of GaAs Grown at Low Temperatures
by Molecular Beam Epitaxy**

A. R. Calawa

**Lincoln Laboratory
Technical Seminar Series,
University of Southern
California,
Los Angeles, California,
20 March 1992**

**Strong Intersubband Absorption by
Photogenerated Carriers in Quantum
Wells**

**E. R. Brown
K. A. McIntosh
K. B. Nichols**

**SPIE Conference,
Somerset, New Jersey,
23-26 March 1992**

**Fabrication of GaInAsP Lasers with
Integrated Microoptics**

**J. N. Walpole
S. H. Groves
Z. L. Liao
L. J. Missaggia**

**DoD Fiber Optics Conference,
McLean, Virginia,
24-27 March 1992**

**Guided-Optical-Wave Modulators for
Microwave Signal Transmission and
Processing**

**R. C. Williamson
L. M. Johnson
G. E. Betts
C. H. Cox III**

Photolithography at 193 nm and Below

M. Rothschild

**Technical Seminar, IBM,
East Fishkill, New York,
26 March 1992**

Optical Interconnects for Digital Systems	D. Z. Tsang	Optics and Quantum Electronics Seminar, Massachusetts Institute of Technology, Cambridge, Massachusetts, 1 April 1992
High- T_c Superconducting Delay Lines, Filters, and Antenna Feed Networks	W. G. Lyons R. S. Withers	Second Symposium on High Temperature Superconductors in High Frequency Fields, Santa Fe, New Mexico, 1-3 April 1992
Measurements and Modeling of Linear and Nonlinear Effects in Striplines	D. E. Oates	
Silylation Technology for 193-nm Lithography	M. A. Hartney	Technical Seminar, Mitsubishi, Hyogo, Japan, 2 April 1992
Two-Dimensional Surface-Emitting Diode Laser Arrays	R. C. Williamson	Lincoln Laboratory Technical Seminar Series, Rensselaer Polytechnic Institute, Troy, New York, 2 April 1992
Resist Alternatives for Sub-0.35- μm Lithography Using Highly Attenuated Radiation	R. R. Kunz M. A. Hartney M. W. Horn M. Rothschild	Topical Meeting on Soft X-Ray Projection Lithography, Monterey, California, 6-8 April 1992
Silylation Technology for 193-nm Lithography	M. A. Hartney	Technical Seminar, Hitachi, Tokyo, Japan, 8 April 1992

Effective Index Series Analysis of Ridge Waveguides with Arbitrarily Sloped Sidewalls

J. P. Donnelly
S. D. Lau

Topical Meeting on Integrated Photonics Research,
New Orleans, Louisiana,
13-15 April 1992

Organometallic Vapor Phase Epitaxy of InGaAs and AlInGaAs Strained Quantum-Well Diode Lasers

C. A. Wang

Lincoln Laboratory Technical Seminar Series,
Massachusetts Institute of Technology,
Cambridge, Massachusetts,
16 April 1992

Time and Temperature Dependence of Phosphorus Vapor Pressure As Measured by a Pressure-Balanced, Sealed-Ampoule Technique

G. W. Iseler
H. R. Clark, Jr.
D. F. Bliss*

Indium Phosphide and Related Compounds,
Newport, Rhode Island,
20-24 April 1992

Buried-Channel CCDs with High Charge Transfer Efficiency and Large Charge Capacity for Low-Temperature Readout of Long-Wavelength Infrared Detectors

A. L. Lattes
B-Y. Tsaur

OE/Aerospace Sensing '92,
Orlando, Florida,
20-24 April 1992

2-5 μm Diode Laser Development

S. J. Eglash
H. K. Choi

High-Power Strained-Layer Tapered Amplifiers

J. N. Walpole
E. S. Kintzer
S. R. Chinn
C. A. Wang
L. J. Missaggia

Fifth Annual Diode Laser Technology Program Conference,
Fort Walton Beach, Florida,
21-23 April 1992

Fast Frequency Modulation of Solid-State Lasers

P. A. Schulz

Optics and Quantum Electronics Seminar,
Massachusetts Institute of Technology,
Cambridge, Massachusetts,
22 April 1992

*Author not at Lincoln Laboratory.

**High- T_c Superconductors at Microwave
Frequencies: Fundamental Properties and
Applications**

D. E. Oates

**Electron Device Group Seminar,
Northeastern University,
Boston, Massachusetts,
27 April 1992**

Diamond Transistors

M. W. Geis

**Materials Research Society
Spring Meeting,
San Francisco, California,
27 April–1 May 1992**

ORGANIZATION

SOLID STATE DIVISION

A. L. McWhorter, *Head*
I. Melngailis, *Associate Head*
E. Stern, *Associate Head*
D. C. Shaver, *Assistant Head*
J. F. Goodwin, *Assistant*

D. J. Ehrlich, *Senior Staff*
N. L. DeMeo, Jr., *Associate Staff*
J. W. Caunt, *Assistant Staff*
K. J. Challberg, *Administrative Staff*

SUBMICROMETER TECHNOLOGY

M. Rothschild, *Leader*
T. M. Lyszczarz, *Assistant Leader*

Astolfi, D. K.
Craig, D. M.
Dennis, C. L.
DiNatale, W. F.
Doran, S. P.
Efremow, N. N., Jr.
Forte, A. R.
Gajar, S. A.*
Geis, M. W.
Goodman, R. B.

Hartney, M. A.
Horn, M. W.
Keast, C. L.
Kunz, R. R.
Maki, P. A.
Melngailis, J.[†]
Sedlacek, J. H. C.
Twichell, J. C.
Uttaro, R. S.

QUANTUM ELECTRONICS

A. Mooradian, *Leader*
P. L. Kelley, *Associate Leader*
A. Sanchez-Rubio, *Assistant Leader*

Aggarwal, R. L.
Cook, C. C.
Daneu, V.
DeFeo, W. E.
DiCecca, S.
Dill, C. D., III
Fan, T. Y.
Hancock, R. C.
Henion, S. R.
Hotaling, T. C.

Hsu, L.*
Jeys, T. H.
Korn, J. A.
Lacovara, P.
Le, H. Q.
Nabors, C. D.
Ochoa, J. R.
Schulz, P. A.
Sullivan, D. J.
Zayhowski, J. J.

ELECTRONIC MATERIALS

A. J. Strauss, *Leader*
B-Y. Tsaur, *Associate Leader*

Anderson, C. H., Jr.
Button, M. J.
Chen, C. K.
Choi, H. K.
Clark, H. R., Jr.
Connors, M. K.
Eglash, S. J.
Fahey, R. E.
Finn, M. C.
Iseler, G. W.

Kolesar, D. F.
Krohn, L., Jr.
Marino, S. A.
Mastromattei, E. L.
McGilvary, W. L.
Nitishin, P. M.
Pantano, J. V.
Reinold, J. H., Jr.
Turner, G. W.
Wang, C. A.

HIGH SPEED ELECTRONICS

R. A. Murphy, *Leader*
M. A. Hollis, *Assistant Leader*
R. W. Chick, *Senior Staff*

Actis, R.
Bergeron, N. J.[‡]
Bozler, C. O.
Brown, E. R.
Calawa, A. R.
Chen, C. L.
Clifton, B. J.[‡]
Goodhue, W. D.
Gray, R. V.
Harris, C. T.
Lincoln, G. A., Jr.
Mahoney, L. J.

Manfra, M. J.
Mathews, R. H.
Mattia, J. P.*
McIntosh, K. A.
McMorran, R. A.
McNamara, M. J.
Nichols, K. B.
Parker, C. D.
Rabe, S.
Rathman, D. D.
Smith, F. W., III
Vera, A.

* Research Assistant

† Part Time

‡ Leave of Absence

ELECTROOPTICAL DEVICES

R. C. Williamson, *Leader*
D. L. Spears, *Assistant Leader*

Aull, B. F.
Bailey, R. J.
Betts, G. E.
Cox, C. H., III
Donnelly, J. P.
Ferrante, G. A.
Golubovic, B.*
Groves, S. H.
Harman, T. C.
Hovey, D. L.
Johnson, L. M.
Liau, Z. L.

Lind, T. A.
Missaggia, L. J.
Mull, D. E.
O'Donnell, F. J.
Palmacci, S. T.
Palmateer, S. C.
Reeder, R. E.
Roussell, H. V.
Tsang, D. Z.
Walpole, J. N.
Woodhouse, J. D.
Yee, A. C.

ANALOG DEVICE TECHNOLOGY

R. W. Ralston, *Leader*
R. S. Withers, *Associate Leader*[†]
T. C. L. G. Sollner, *Assistant Leader*
A. C. Anderson, *Senior Staff*
R. M. Lerner, *Senior Staff*[†]

Arsenault, D. R.
Bhushan, M.[‡]
Boisvert, R. R.
Brogan, W. T.
Delin, K. A.
Denneno, A. P.
Denneno, J. M.
Fitch, G. L.
Green, J. B.
Holtham, J. H.
Lyons, W. G.

Macedo, E. M., Jr.
Minnick, R. G.
Oates, D. E.
Sage, J. P.
Seaver, M. M.
Slattery, R. L.
Tam, K.*
Westerheim, A. C.*
Whitley, D. B.
Yu-Jahnes, L. S.*

MICROELECTRONICS

E. D. Savoye, *Leader*
B. B. Kosicki, *Assistant Leader*
B. E. Burke, *Senior Staff*
A. M. Chiang, *Senior Staff*

Chuang, M. L.*
Collins, I. K.
Daniels, P. J.
Doherty, C. L., Jr.
Dolat, V. S.
Donahue, T. C.
Durant, G. L.

Felton, B. J.
Gregory, J. A.
Hurley, E. T.
Johnson, B. W.
Johnson, K. F.
LaFranchise, J. R.

Loomis, A. H.
McGonagle, W. H.
Mountain, R. W.
Percival, K. A.
Pichler, H. H.
Reich, R. K.
Young, D. J.

* Research Assistant
† Part Time
‡ Leave of Absence

1. ELECTROOPTICAL DEVICES

1.1 EXTERNAL-MODULATOR ANALOG LINK WITH OPTICAL AMPLIFIER

External-modulator analog fiber-optic links [1] have been widely investigated for applications such as radar and CATV signal distribution. The advent of high-gain optical amplifiers offers the prospect of greatly improved link performance along with expanded design flexibility. Recently, we have examined analog links both theoretically and experimentally using an interferometric external modulator and an erbium-doped fiber amplifier. Unlike the case for conventional external-modulator links without an amplifier, biasing the modulator near the transmission null point in amplified links provides substantial performance advantages. External-modulator links using diode laser sources and high-gain amplifiers can provide a high signal-to-noise ratio (SNR) that remains constant over a wide range of insertion loss between the amplifier and receiver.

The generic link design considered here, shown in Figure 1-1, comprises a transmitter consisting of a CW optical source, an external interferometric intensity modulator, and an optical amplifier of gain G , followed by an optical path of transmission T , and an optical receiver. In conventional links, the modulator bias point θ_b is set at 90° , the half-power point, to maximize the linear response and eliminate even-order nonlinearities. However, operating at the half-power point in amplified links can lead to optical amplifier saturation at moderate values of gain, which could limit overall link performance. This is particularly true for amplifiers placed near the transmitter. Operating closer to the transmission null point, $\theta_b = 180^\circ$, allows the use of high-gain amplifiers and results in improved system dynamic range and noise figure, particularly for suboctave links where second-harmonic distortion is not an issue. (Setting θ_b exactly at 180° would eliminate the linear response.) Near the transmission null point, the ratio of modulated optical power to average power is greatly increased for a given modulator drive power. Also, for an interferometric modulator, relative third-order nonlinearities are independent of the bias point.

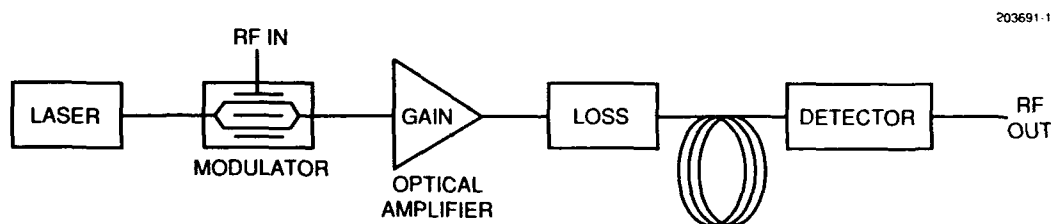


Figure 1-1. Schematic layout of external-modulator analog link with optical amplifier.

It is useful to focus on the SNR as a link figure of merit. Given the SNR for a known modulator drive power, the link noise figure and the intermodulation-free dynamic range are readily determined. For an amplified link, the highest SNR is obtained in the limit where signal-spontaneous beat noise domi-

nates. This SNR limit is independent of G and T and is therefore of particular interest for systems with small T , such as multipoint links with high fan-out loss, which would otherwise be dominated by receiver thermal noise. A similar result is obtained for operation in the limit where relative intensity noise (RIN) dominates.

For both amplified and nonamplified experimental links, the transmitter consisted of a CW 1546-nm wavelength distributed-feedback laser and a LiNbO_3 interferometric modulator. The modulator was driven by a -50-dBm signal at 20 MHz with θ_B set at 140° and 90° for the amplified and nonamplified links, respectively. In the amplified link, the modulator output was connected to an erbium-doped fiber amplifier [2], which was pumped from the input end by 22 mW of power from a pair of 980-nm diode lasers. Small-signal amplifier gain and the -3-dB gain compression point were determined to be 26 dB and 3.6 dBm, respectively. A tunable optical filter was placed after the amplifier to minimize the effect of amplified spontaneous emission. For both links, measurements of SNR were performed as a function of the optical transmission T , which was set by adjusting an optical attenuator in front of the photodetector. The results are shown in Figure 1-2. The amplified link noise for the lower loss values is dominated by beat noise and RIN. In this regime the SNR is independent of T as expected. For $T = -12$ dB, the SNR is about 52 dB. At higher loss values the thermal noise becomes significant and the SNR declines. Without an amplifier the SNR is dominated by thermal noise over most of the indicated range of T . The RIN becomes significant only for the lowest-loss links.

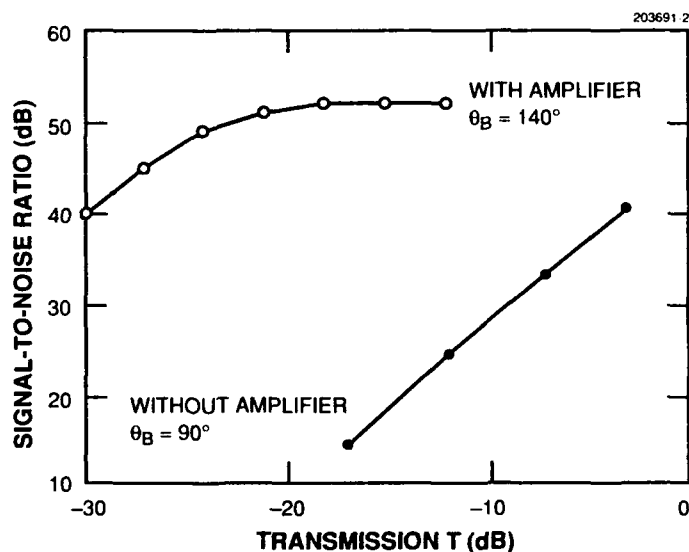


Figure 1-2. Plot of link SNR vs optical transmission T . For the link with an amplifier, T is the transmission between the amplifier output and the receiver. For the link without an amplifier, T represents the transmission between the modulator output and the receiver.

The results indicate that high SNR can be maintained in amplified links over more than a 20-dB range of optical attenuation between the amplifier and receiver. Most important, this is obtained using only a diode laser source. Further improvement is expected with reduced laser noise and increased transmitter power.

L. M. Johnson
B. R. Hemenway
H. V. Roussel

1.2 LARGE-NUMERICAL-APERTURE MICROLENSES FABRICATED BY ONE-STEP ION-BEAM ETCHING AND MASS-TRANSPORT SMOOTHING

Semiconductor microlenses fabricated by mesa etching and mass-transport smoothing have high indices and accurate profiles and are potentially well suited for large numerical-aperture microoptical applications and monolithic optoelectronic integration [3]. However, the repeated lithography and etching needed for the multilevel mesa structure can become time-consuming. In this work, we describe a new technique in which only a single deep etch is required.

As illustrated in Figure 1-3, the lateral mass distribution needed for the lens profile is accurately provided by the variation of the mesa width. Such a structure has been realized by ion-beam-assisted etching, which is capable of forming deep grooves of high aspect ratio regardless of the crystallographic orientation [4]. Figure 1-4(a) shows a scanning electron microscope (SEM) photograph of an etched structure in a GaP substrate. It has an overall diameter of 126 μm and a height of 8.6 μm and is designed for an $f/1$ spherical lens.

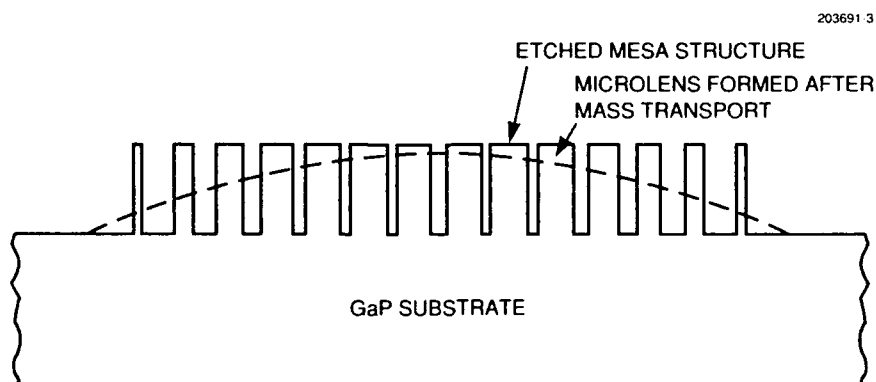


Figure 1-3. Present technique of microlens fabrication by one-step ion-beam etching and mass-transport smoothing.

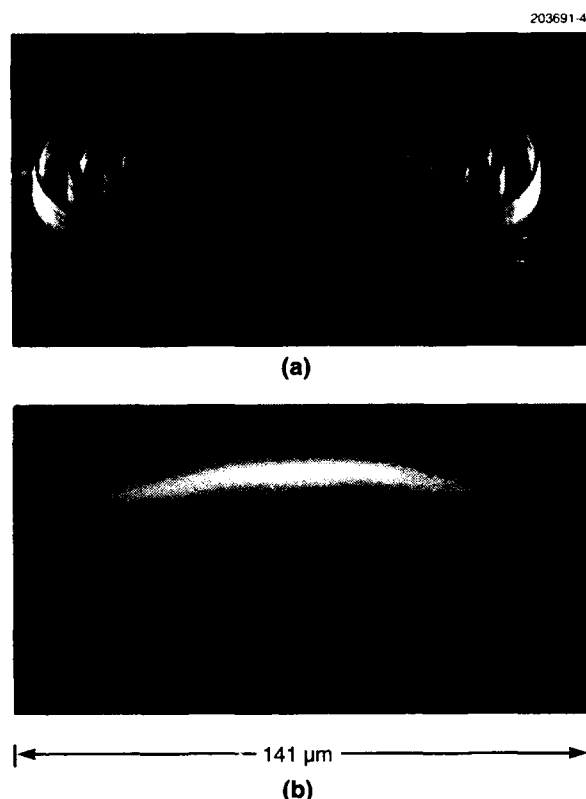


Figure 1-4. Scanning electron micrograph perspective views of (a) a mesa structure produced by ion-beam-assisted etching and (b) a microlens formed after mass-transport smoothing.

Mass transport was carried out in a furnace system with H_2 and PH_3 flow. The etched wafer was sandwiched between a pair of SiO_2 -coated GaP protecting wafers and placed in a quartz container. (The graphite container employed previously [5] became porous and embrittled, especially for the temperature range used in the present work.) Lower temperatures of 900–950°C were first used for ~ 200 h to partially smooth the deeply etched structure at a moderate rate. Higher temperatures up to 1130°C were then used for ~ 60 h to complete the smoothing.

The microlens formed after mass transport is shown in Figure 1-4(b), and a stylus surface profile of the same lens is depicted in Figure 1-5. This measured profile is indeed very close to a spherical one, as designed. Figures 1-6(a) and 1-6(b) show optical micrographs of the etched mesa and the microlens formed. Sharp images have been obtained from the lens both by using reflected [Figure 1-6(c)] and transmitted light (the technique for image formation is described in [3]). This result agrees with the accurate lens profile in Figure 1-5 and, further, demonstrates good optical quality. However, a small deviation from the exact circular symmetry can be detected by a close examination of Figure 1-6(b). This deviation is due to the strong crystallographic orientational dependence in the initial stage of mass transport and can probably be minimized by improved mesa patterns and mass-transport conditions.

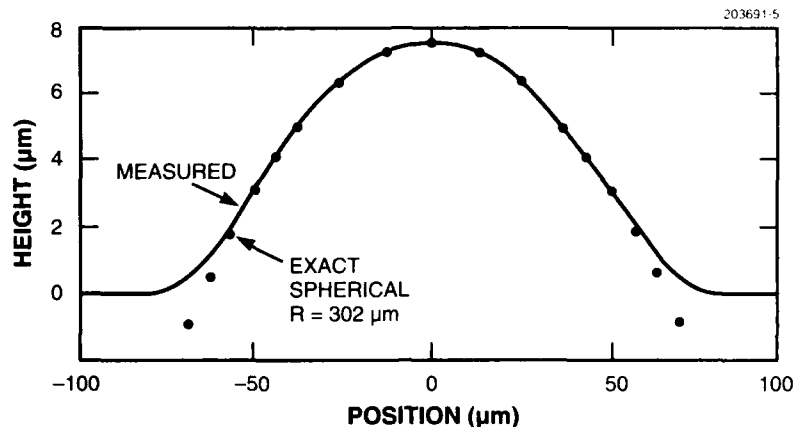


Figure 1-5. Stylus surface profile of the fabricated microlens (solid curve) compared with a calculated spherical profile (dots).

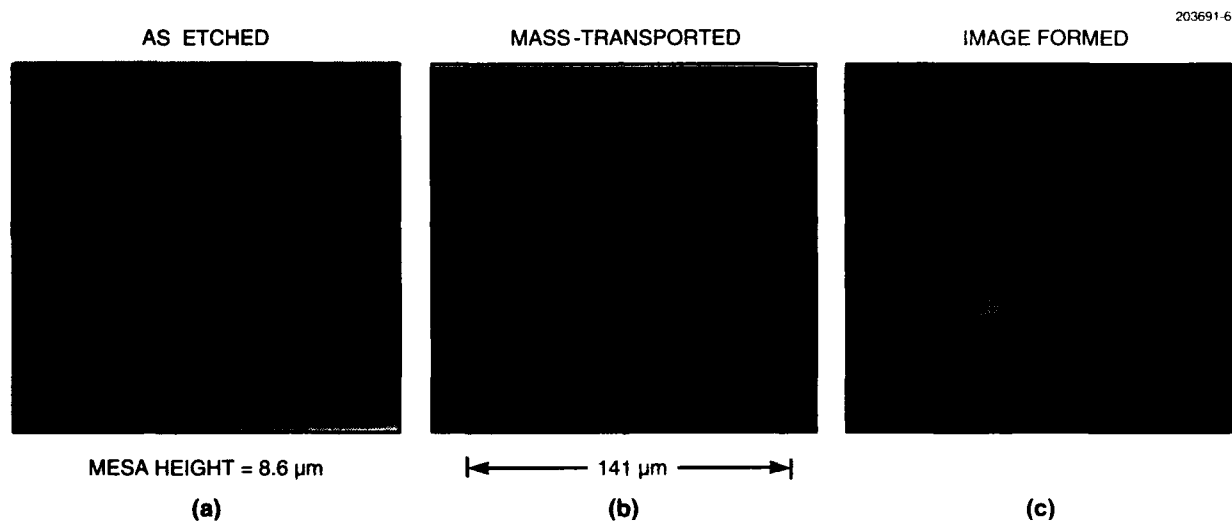


Figure 1-6. Optical micrographs of (a) an etched mesa structure, (b) a microlens formed after mass transport, and (c) an image formed by the microlens surface. The vertical striations in (b) are the partially focused image of the tungsten filament in the microscope light source.

The lens accuracy also depends strongly on the lithographic mask, in which feature sizes on the order of 1 μm are needed for $f/1$ lenses. Although such mask patterns have been rather accurately produced by electron-beam lithography, small deviations can be introduced by the pattern effect in the electron-beam exposures. This problem can be corrected by design iterations. On the other hand, a constant universal error in all mesa widths across the entire structure (introduced by subsequent lithographic inaccuracies or erosion of the SiO_2 mask during the ion-beam etching) will only lead to an overall vertical shift of the entire lens profile and a resulting distortion near the lens perimeter [6]. Another major factor affecting the lens precision is the etched depth, which was not completely reproducible in the present experiment. Correction etches were needed in achieving a precision depth.

In conclusion, fabrication of large-numerical-aperture microlenses by one-step etching and mass transport has been demonstrated. This technique is potentially very simple and highly accurate. Additional work is needed for more detailed evaluation of the method, and for its further improvement and development for other advanced microoptical structures.

Z. L. Liao
D. E. Mull
C. L. Dennis

1.3 GaInAsP STRAINED LAYERS FOR GaAs-BASED DIODE LASERS

The $\text{Ga}_x\text{In}_{1-x}\text{As}_y\text{P}_{1-y}$ alloys with x and y paired to obtain lattice matching to GaAs (referred to as GaInAsP/GaAs) offer an interesting alternative to the AlGaAs alloys for device applications. We have developed the organometallic vapor phase epitaxial (OMVPE) growth of these materials and applied it to structures for diode lasers. Previously, two types of single-quantum-well (SQW) separate-confinement heterostructure (SCH) lasers operating at the 980-nm wavelength were demonstrated. Both had an $\text{In}_{0.2}\text{Ga}_{0.8}\text{As}$ strained-layer SQW and $\text{Ga}_{0.5}\text{In}_{0.5}\text{P}$ (GaInP) cladding layers, but the optical confinement layers differed. In the first case, GaAs ($E_g = 1.4$ eV) was used, primarily for simplicity of crystal growth, and diode lasers with very low threshold current densities, $J_{th} < 100$ A/cm², were obtained [7]. In the second structure, a higher-bandgap optical-confinement material was grown using a lattice-matched GaInAsP alloy ($E_g = 1.7$ eV), and differential quantum efficiencies greater than 93%, which are among the highest measured for any diode lasers, were achieved [8].

Here, we present a further advance in the development of the GaInAsP/GaAs materials with the first reported strained-GaInAsP quantum wells. A schematic cross section of the strained SQW SCH used is shown in Figure 1-7. It differs from an actual diode laser structure for emission at 830 nm in that the GaInP cladding layers are nonintentionally doped and are about half the thickness. Also, a top GaAs contact layer is omitted. The alloy composition of the strained-layer quantum well, with $x = 0.6$ and $y = 0.4$ estimated from a quaternary interpolation scheme [9], has been chosen to give 830-nm emission and the same biaxial compression ($\sim 1.4\%$) as the $\text{In}_{0.2}\text{Ga}_{0.8}\text{As}$ alloy for the 980-nm lasers. With minor alloy changes, operation at 808 nm to pump Nd:YAG solid state lasers should be obtainable.

In previous work on strained layers, compressive strain has been introduced into binary or ternary materials by adding excess indium. Group III elements such as indium are relatively easy to control because their atomic fractions in the solid are about the same as their precursor volume fractions in the vapor. Here, however, the most tractable approach for the introduction of compressive strain is to modify a lattice-matched GaInAsP alloy by increasing the As fraction. This presents some challenge because the group V vapor-to-solid incorporation ratio is quite different from unity and it varies rapidly with composition.

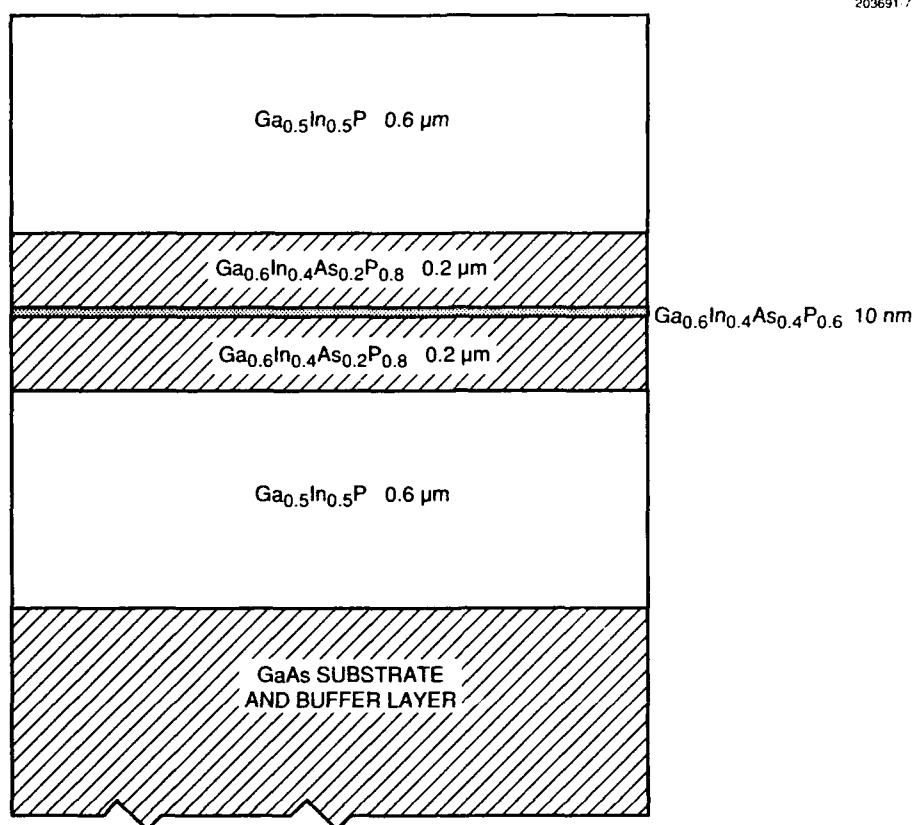


Figure 1-7. Undoped separate-confinement heterostructure with strained GaInAsP quantum well.

A second difficulty occurs with the strain (and composition) determination. X-ray diffraction is normally used to measure strain and deduce the composition of nearly lattice-matched alloys. Yet, the detectable single-layer thickness for that technique (~ 100 nm) is much larger than the critical thickness for the onset of lattice relaxation (< 20 nm) in these strained layers.

We have adopted a two-step procedure to deal with these problems and to converge upon a composition that gives the desired strain and photon energy. To establish the strain, or biaxial compression, a structure has been synthesized by periodically growing the thin strained layer between thick (~ 50 nm) GaAs spacer layers until there is a sufficient total strained-alloy thickness to be detected by x-ray diffraction. A double-crystal rocking curve for such a structure with eight periods is shown in Figure 1-8. As described previously [10], accurate determination of InGaAs strained-layer compositions

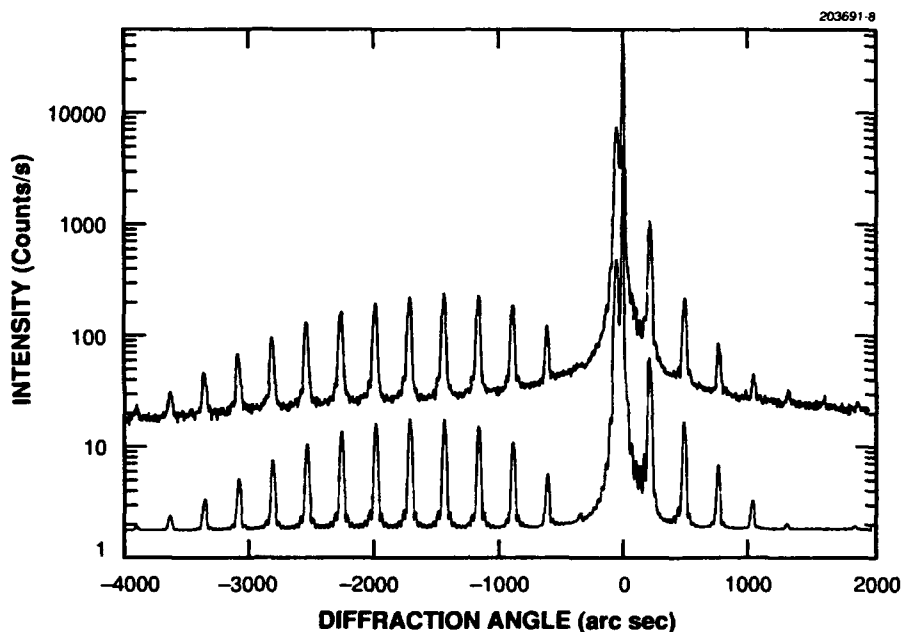


Figure 1-8. Rocking curve of eight-period structure with $\text{Ga}_x\text{In}_{1-x}\text{As}_y\text{P}_{1-y}$ strained layer and 590-nm GaAs spacer layer. The lower curve, shifted downward by an order of magnitude for visualization purposes, is a simulated rocking curve for $x = 0.60$ and $y = 0.44$, a 9.8-nm strained-layer thickness, and a 59-nm GaAs thickness. The reflection is (004) with Cu K_α radiation, and the diffraction angle origin is taken at the Bragg angle for GaAs.

were made by comparing measured and simulated rocking curves of the type shown in Figure 1-8. With the quaternary materials, establishing a composition is less certain. However, the amount of strain is accurately determined by the fitting process, and this is actually the quantity needed to progress toward growth of the desired device structure.

In the second step of the iterative process, the emission wavelength has been established by incorporating the strained GaInAsP into the structure of Figure 1-7 and measuring the photoluminescence (PL). The PL data from a sample with the desired strain and emission are shown in Figure 1-9. The peak at 1.88 eV is due to the GaInP cladding, the one at 1.74 eV is due to the optical confinement alloy, and the one of high intensity at 1.495 eV (829 nm) is due to the GaInAsP quantum well.

The x-ray and PL data suggest that the structures grown with the strained-GaInAsP layers are of high crystalline quality. In the x-ray case, as shown in Figure 1-8, there is close agreement between the experimental rocking curve and the simulated rocking curve for an ideal structure. For the PL, the intensities of the peaks compare very favorably with those from structures that preceded the 980-nm diode lasers.

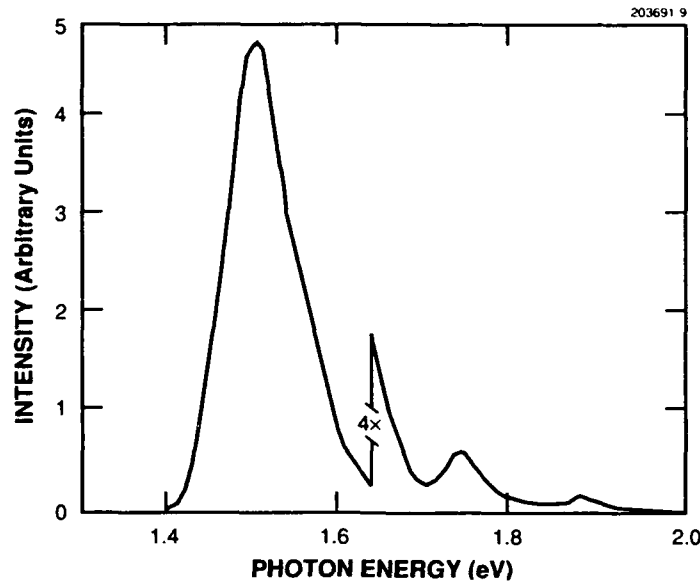


Figure 1-9. Room-temperature photoluminescence from the structure of Figure 1-7. Excitation is at 514 nm, and a photomultiplier with S-1 response is used for detection.

Doped structures have been grown for diode lasers and are presently being processed for broad-area characterization.

S. H. Groves
A. Napoleone
D. R. Calawa

1.4 RIDGE WAVEGUIDE LASERS FOR HIGH-SPEED FREE-SPACE OPTICAL INTERCONNECTIONS

Free-space optical interconnections are of interest as a high-speed replacement for electrical interconnections in digital computers [11],[12]. Short-distance parallel point-to-point interconnections used as high-density connections between boards require an array of diode lasers or modulators that can be focused onto an array of detectors. Efficient low-threshold lasers that can be directly driven by digital logic simplify the optical interconnections. The sources used in optical interconnection systems should have long operational lifetime, narrow beam divergence, and the capability to operate over a large temperature range in order to eliminate the need for thermoelectric coolers. Strained-layer InGaAs lasers have a T_0 of about 180 K, and their power output is less sensitive to temperature variations than that of either GaAs or long-wavelength InP-based lasers. InGaAs/AlGaAs ridge waveguide diode lasers have been described previously [13]. This report details the developments and improvements in these lasers and their threshold and efficiency performance characteristics.

Initial ridge waveguide lasers were fabricated in InGaAs/AlGaAs material with a graded-index SCH double-quantum-well (DQW) structure with an InGaAs quantum-well active region that was grown on n^+ GaAs by OMVPE [14]. A cross section of the ridge waveguide structure is shown in Figure 1-10. This particular DQW structure has a divergence angle of 40° full width at half-maximum (FWHM) based on pulsed measurements of broad-area lasers. The ridge is fabricated using a photolithographic liftoff process to pattern a 100-nm-thick Ni stripe mask on the wafer, and ion-beam-assisted etching to achieve straight sidewalls and maintain a depth uniformity of $< 3\%$ across a wafer. An SiO_2 insulating layer is pyrolytically deposited, and a contact window is opened on the ridge by standard photolithographic techniques. A patterned Ti/Pt/Au contact is applied by sputtering and liftoff. This metallization serves as the p contact and bonding pad for the device. After thinning the wafer to a thickness of $75\ \mu\text{m}$, n -type contact metals (Ge/Au/Ni/Au) are evaporated on the back side and alloyed at 420°C . Laser bars containing 40–50 lasers each were cleaved into several lengths in the range $200\text{--}500\ \mu\text{m}$. Lasers with nominal ridge widths that vary from 2 to $5.5\ \mu\text{m}$ in $0.5\text{-}\mu\text{m}$ increments were initially fabricated to determine the effect of ridge width.

Figure 1-11 shows plots of threshold current I_{th} and differential quantum efficiency η_d as a function of nominal ridge width from two $500\text{-}\mu\text{m}$ -long laser bars. The data were obtained from light output vs

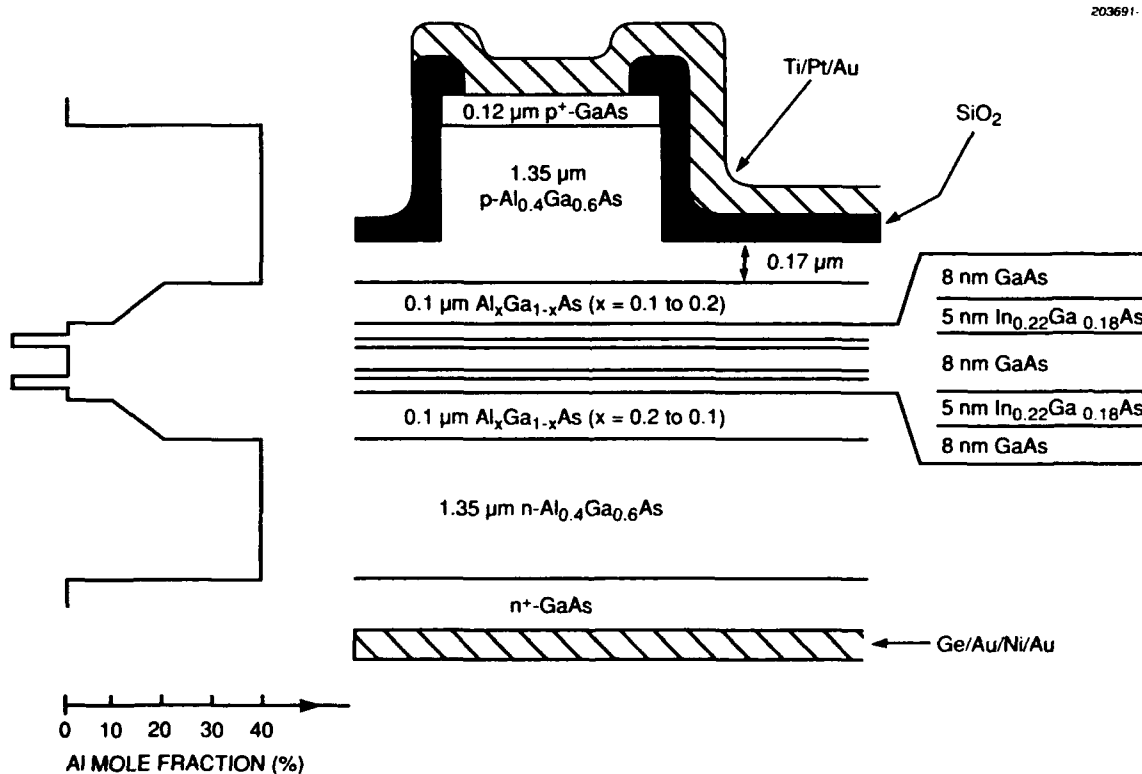


Figure 1-10. Cross-sectional schematic diagram of InGaAs/AlGaAs ridge waveguide laser structure showing the double-quantum-well active region.

pulsed current measurements (300-ns pulses at 1 kHz). Although the data show considerable scatter for the narrower ridge devices, the threshold current generally increases with increasing ridge width. The I_{th} for these uncoated 500- μm lasers was typically below 10 mA for all ridge widths. Only one laser (a 5- μm -wide ridge laser not plotted) out of the 70 on the two bars had $I_{th} > 15$ mA. The lowest I_{th} , 5.3 mA, was obtained on a laser with a 2.5- μm -wide ridge. The η_d averaged about 40% per facet for all ridge widths. Far-field data obtained from this wafer indicate a beam divergence between 14° and 18° FWHM for all ridge widths. Lowest-order lateral mode operation was observed for all lasers with nominal ridge widths ≤ 4.5 μm , while a higher-order mode was observed at 5 and 5.5 μm .

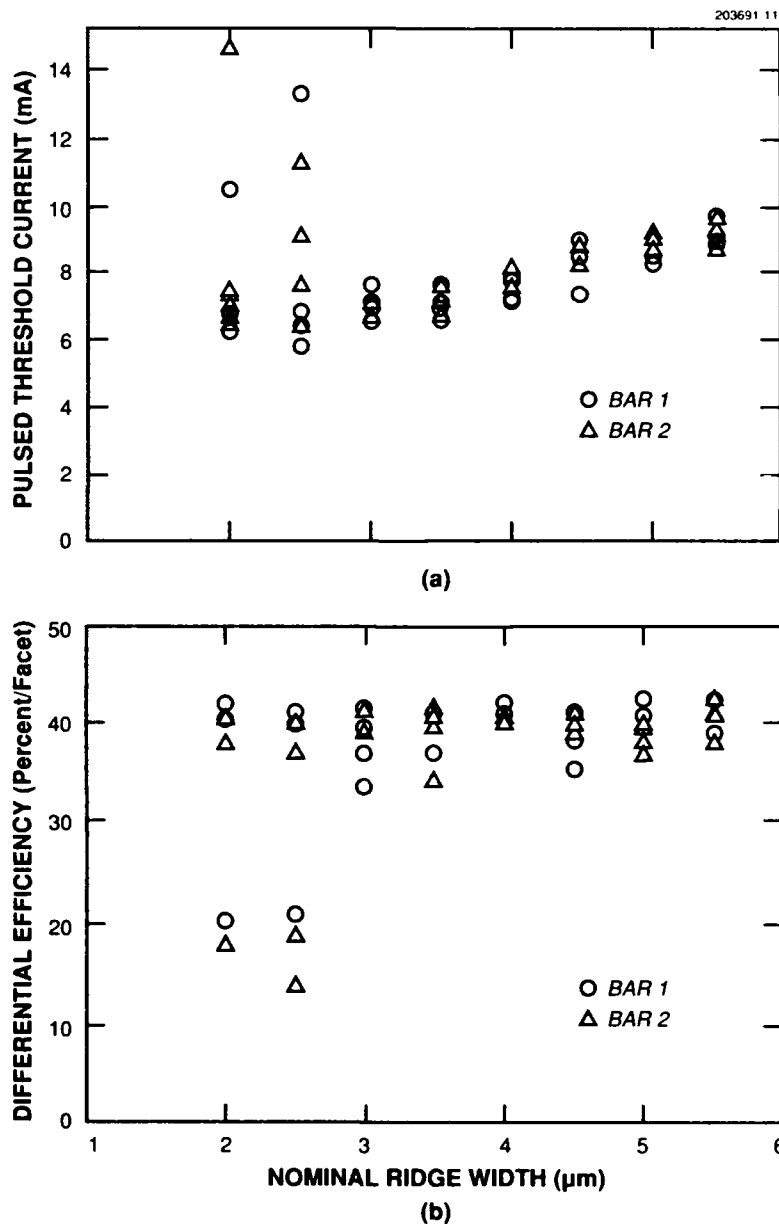


Figure 1-11. Plots of (a) pulsed threshold current and (b) differential quantum efficiency, both as a function of nominal ridge width for two 500- μm -long, uncoated ridge waveguide laser bars.

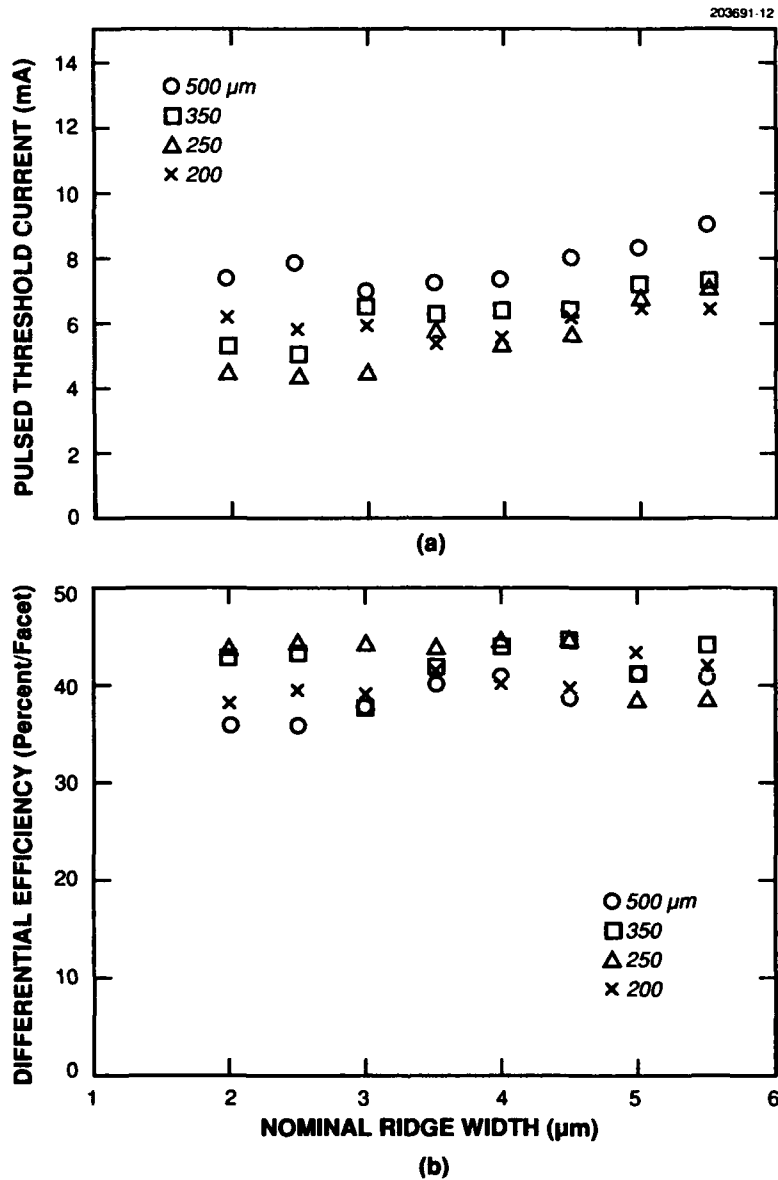


Figure 1-12. Plots of (a) average pulsed threshold current and (b) average differential quantum efficiency, both as a function of nominal ridge width for 200-, 250-, 350-, and 500- μm -long, uncoated ridge waveguide laser bars. The data for the 500- μm -long laser bar represent an average of all devices from the better bar (1) in Figure 1-11.

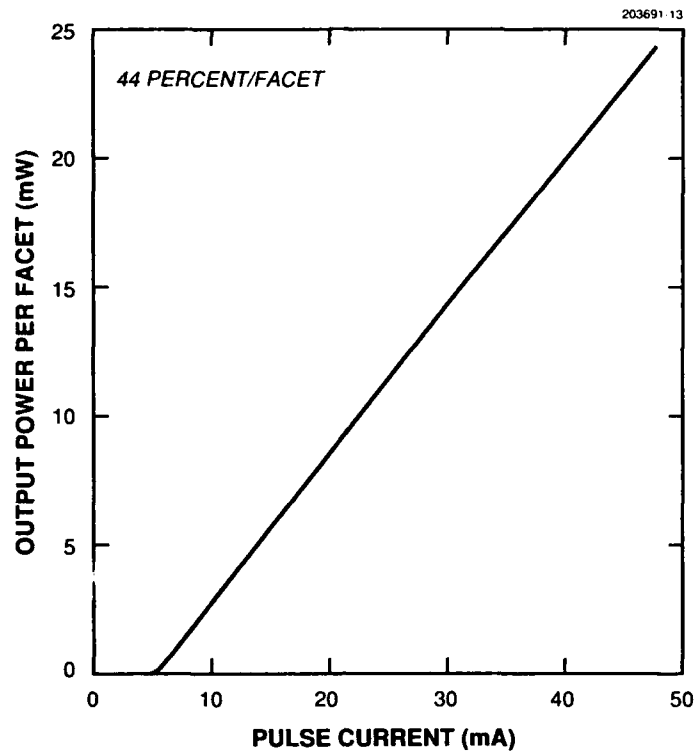


Figure 1-13. Output power per facet vs pulse input current for a 2.5- μm -wide, 200- μm -long uncoated ridge waveguide laser.

Cleaved bars with lengths of 200, 250, and 350 μm were also tested. A summary of the data is plotted in Figure 1-12, where each point represents an average value of I_{th} or η_d for all lasers having that particular ridge width (typically four or eight of each size). The shorter, narrower devices generally had the lowest threshold currents. The 250- and 350- μm devices routinely exhibited threshold currents ≤ 5 mA for the 2- and 2.5- μm ridge widths. The average η_d per facet lies between 35 and 45% for all lasers. The output power vs current characteristic for a 2.5- μm -wide laser is shown in Figure 1-13. For this uncoated laser, I_{th} is 4.5 mA and η_d is 44% per facet. Arrays of 2- μm -wide ridge lasers with high reflectivity coatings on one facet are in process.

J. D. Woodhouse	J. P. Donnelly
D. Z. Tsang	R. J. Bailey
C. A. Wang	K. Rauschenbach

REFERENCES

1. G. E. Betts, L. M. Johnson, C. H. Cox III, and S. D. Lowney, *IEEE Photon. Technol. Lett.* **1**, 404 (1989).
2. The fiber was provided by GTE Laboratories.
3. Z. L. Liao, V. Diadiuk, J. N. Walpole, and D. E. Mull, *Appl. Phys. Lett.* **52**, 1859 (1988); **55**, 97 (1989).
4. M. W. Geis, G. A. Lincoln, N. Efremow, and W. J. Piacentini, *J. Vac. Sci. Technol.* **19**, 1390 (1981).
5. Z. L. Liao, *Appl. Phys. Lett.* **58**, 1869 (1991).
6. R. C. Williamson, private communication.
7. Z. L. Liao, S. C. Palmateer, S. H. Groves, J. N. Walpole, and L. J. Missaggia, *Appl. Phys. Lett.* **60**, 6 (1992).
8. Solid State Research Report, Lincoln Laboratory, MIT, 1992:1, p. 7; S. H. Groves, J. N. Walpole, and L. J. Missaggia, *Appl. Phys. Lett.* **61**, 255 (1992).
9. R. E. Nahory, M. A. Pollack, W. D. Johnston, Jr., and R. L. Barns, *Appl. Phys. Lett.* **33**, 659 (1978).
10. Solid State Research Report, Lincoln Laboratory, MIT, 1990:3, p. 9.
11. D. Z. Tsang, *Appl. Opt.* **29**, 2034 (1990).
12. D. Z. Tsang, *Lincoln Lab. J.* **4**, 31 (1991).
13. H. K. Choi, C. A. Wang, and S. J. Eglash, *Lincoln Lab J.* **3**, 395 (1990).
14. C. A. Wang, *Lincoln Lab. J.* **3**, 3 (1990).

2. QUANTUM ELECTRONICS

2.1 DIODE-PUMPED MICROCHIP LASERS ELECTROOPTICALLY *Q* SWITCHED AT HIGH PULSE REPETITION RATES

Using a diode-pumped, electrooptically *Q*-switched Nd:YAG microchip laser, we have obtained what we believe to be the shortest *Q*-switched pulses ever obtained from a laser, the highest rate of repetitive *Q* switching from any laser with the exception of semiconductor diode lasers, and the highest peak power from a laser pumped by a single diode. In addition, the output of the *Q*-switched microchip laser is single-frequency, single-polarization, and near diffraction limited.

The *Q*-switched microchip laser discussed here consists of a 532- μm -long piece of 1.8-wt% Nd:YAG bonded to a 904- μm -long piece of LiTaO₃ [1]. Both materials were polished flat and parallel on the two faces normal to the optic axis. The unbonded pump-side face of the Nd:YAG was dielectrically coated to both transmit the pump light and be highly reflective at the oscillating wavelength (1.064 μm). A partially transmitting mirror between the two materials had a reflectivity of 95% at 1.064 μm and reflected the pump light, to allow double-pass absorption of the pump. The opposite face of the LiTaO₃ was coated for 50% reflectivity at 1.064 μm . The LiTaO₃ was oriented with its *c*-axis orthogonal to the cavity axis. Electrodes were deposited on the two faces of the LiTaO₃ normal to the *c*-axis, with an electrode spacing of ~ 1 mm.

In these experiments, the electrooptically *Q*-switched microchip laser was pumped with a butt-coupled, 500-mW, 808-nm diode laser. The pump absorption efficiency of the device was $\sim 31\%$. *Q* switching was performed by applying a high-voltage pulse (200–800 V) of 100-ns duration to the LiTaO₃ at repetition rates up to 500 kHz. (The highest pulse repetition rate, 500 kHz, was limited by the high-voltage electronics used.) At each pulse repetition rate, the magnitude of the high-voltage pulse, the dc bias applied to the LiTaO₃, and the temperature of the device were chosen to minimize the duration of the output pulse.

During *Q*-switched operation, the output of the microchip laser maintained its single-frequency, single-polarization, near-diffraction-limited performance [2]. The pulse width (full width at half-maximum) increased from < 300 ps at 5 kHz to 13 ns at 500 kHz, as shown in Figure 2-1. For pulse repetition rates below 5 kHz, the pulse width was nearly independent of repetition rate. At these low repetition rates, the spontaneous relaxation time limits the effective pump period and therefore the inversion density, which determines the pulse width [3]. Above 5 kHz the pulse width was nearly proportional to the pulse repetition rate and was in excellent agreement with theory [3].

The time-averaged output power from the microchip laser was between 50 and 57 mW for pulse repetition rates between 10 and 500 kHz, and was relatively independent of the repetition rate. At 5 kHz and below, the time-averaged output power of the microchip laser decreased in a manner consistent with the spontaneous relaxation time. At low repetition rates, the pulse energy of the *Q*-switched microchip laser reached several microjoules, and the peak pulse power reached tens of kilowatts. The pulse-to-pulse amplitude jitter was $< 0.5\%$, the resolution of our instruments. The timing jitter between the input

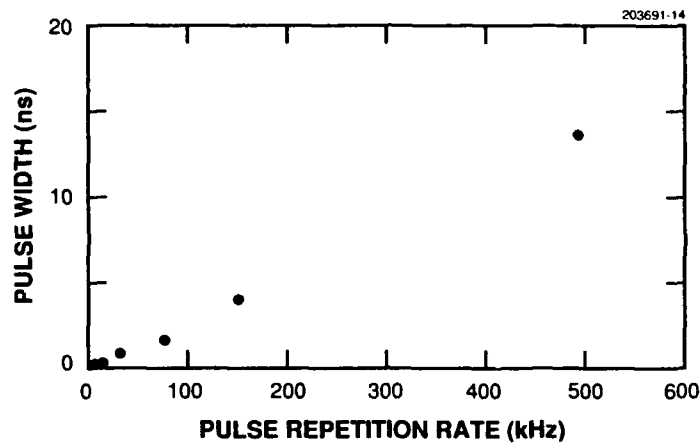


Figure 2-1. Full width at half-maximum of the output pulses obtained from a 1.064- μm , diode-pumped, electrooptically *Q*-switched Nd:YAG microchip laser as a function of pulse repetition rate.

electrical trigger and the output optical pulse, < 0.5 ns, was a result of the intermediate electronics. Table 2-1 summarizes the pulse characteristics.

The high peak power of the output of the *Q*-switched microchip laser at low repetition rates allows for efficient frequency doubling to obtain single-frequency green pulses. By simply placing a properly oriented, 7-mm-long crystal of KTP ~ 3 mm from the output facet of the *Q*-switched microchip laser (with no intervening optics), we were able to obtain 15% doubling efficiency at a pulse repetition rate of 25 kHz.

In a demonstration of another potential application of *Q*-switched microchip lasers, we used one to cut 6- μm -wide lines in 30-nm-thick layers of platinum-gold on glass substrates. At a pulse repetition rate of 100 kHz, individual *Q*-switched pulses deposited sufficient thermal energy to ablate a 6- μm -diam hole in the metallization.

The geometry of electrooptically *Q*-switched microchip lasers allows them to be inexpensively produced as individual devices or in one- and two-dimensional arrays. The complete device fits into a package approximately the size of a conventional diode laser package. Potential applications of the device include LIDAR, nonlinear frequency generation, and laser cutting.

J. J. Zayhowski	C. C. Cook
C. D. Dill III	T. C. Hotaling
J. L. Daneu	

TABLE 2-1
**Characteristics of the Output Pulses from a 1.064- μ m, Diode-Pumped,
Electrooptically Q-Switched Nd:YAG Microchip Laser**

Pulse Rate (kHz)	Pulse Width* (ns)	Time-Averaged Power (mW)	Pulse Energy† (μ J)	Peak Power‡ (W)
5	0.27	34	6.80	25 185
10	0.43	50	5.00	11 627
30	0.91	53	1.77	1941
75	2.0	55	0.73	367
150	4.1	57	0.38	93
500	13.3	50	0.10	7.5
CW	—	55	—	—

* Pulse width measurements (full width at half-maximum) at 5, 10, and 30 kHz were obtained by deconvolving the measured 420-ps impulse response of the detector-oscilloscope system from the observed 500-, 600-, and 1000-ps oscilloscope traces, respectively.
† Pulse energy was calculated from the pulse repetition rate and time-averaged power.
‡ Peak power was calculated from the pulse energy and pulse width.

2.2 HIGH-POWER, CONTINUOUS-WAVE MICROCHIP LASER ARRAY

Microchip lasers consist of monolithic flat-flat cavities formed by a short length of gain material with dielectric cavity mirrors deposited directly on the surfaces [2],[4],[5]. These lasers have been demonstrated with good efficiency and single-frequency operation in various ion:host combinations [2],[6],[7]. Q-switched operation has also been demonstrated [8]. It is possible to fabricate a thin, large-area, flat-flat resonator structure and to pump with a two-dimensional diode laser array so that a corresponding array of solid-state microchip emitters is formed. The output beams of such a laser array will be parallel and will overlap in the far field, with a divergence equal to that of a single element. Microchip laser arrays thus offer the ability to scale the output power significantly while maintaining many of the properties of the single device. In addition, such arrays have the potential to be robust, compact, and manufacturable devices.

To achieve high-power, CW operation, we employed a commercial two-dimensional diode laser pump array, comprising five laser bars with twelve 200- μ m-wide stripes on 800- μ m centers, each bar nominally capable of emitting 10 W CW and having a standard deviation of wavelength of 0.84 nm. The bars are stacked with a 2-mm pitch and are fitted with cylindrical microlenses to collimate their emission. The principal function of the lenslets is to concentrate the pump light so as to establish adequate local heating to preserve the index profile required for stable-mode operation under CW conditions. A

12 × 12 × 2-mm, 1.1% Nd:YAG microchip slab is bonded to a 15 × 15 × 2-mm sapphire heatsink, as shown in Figure 2-2. The geometry of the sapphire heatsink was chosen to promote longitudinal heat flow, and to minimize large-scale transverse thermal gradients and edge effects that tend to destabilize and smear out the microchip element spatial modes. The pump-side surface of the microchip slab is coated with a high-reflectivity dielectric stack for 1.064 μm that is highly transmitting (> 90%) for the 809-nm pump light. The back surface of the microchip has a reflectivity of 98% at 1.064 μm and is highly reflective for the pump light as well, resulting in a double pass of the pump for greater efficiency. The pump-side surface of the sapphire is uncoated, and the back surface is antireflection coated for 1.064 μm . There is no need to register the microchip slab to the diode array. The positions of the lasing modes are self-aligning, so it is possible to translate the slab in the transverse plane without measurable effect on either the output power or beam quality.

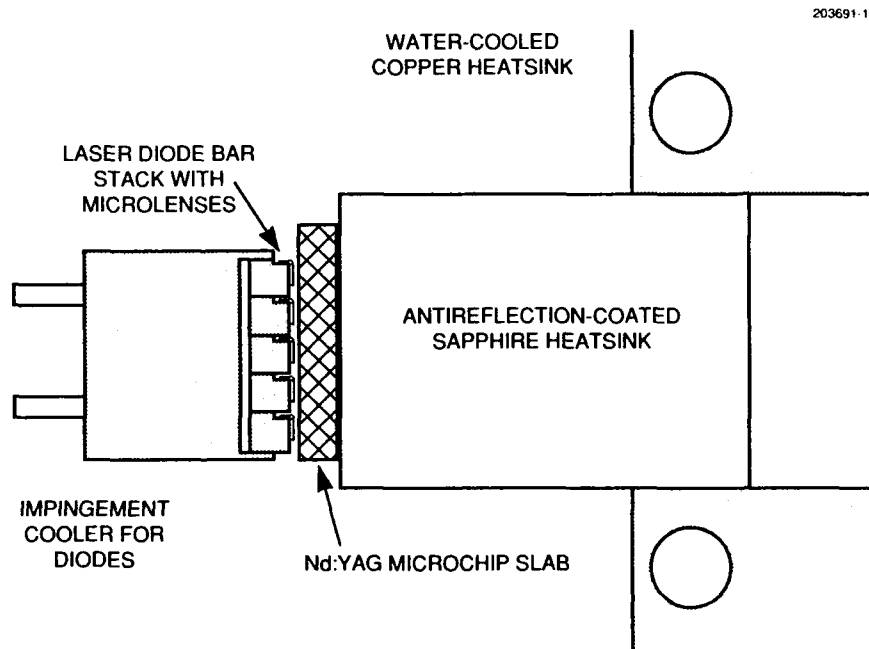


Figure 2-2. Schematic diagram of the experimental setup. The Nd:YAG microchip slab is bonded to the sapphire heatsink, which in turn is heatsunk by the water-cooled copper collar at the output end. This arrangement minimizes transverse thermal gradients and edge effects in the Nd:YAG slab.

The output power of the solid-state microchip laser array as a function of incident pump power is shown in Figure 2-3. All measurements were taken using a thermopile power meter. For each setting of the diode array injection current the temperature of the diode pump array was adjusted so as to keep the pump wavelength near its optimum of ~ 809 nm. The observed average slope efficiency of the ensemble was 32.5%. The highest measured power from the microchip array was 9.8 W with a pump power of

38.5 W and a diode array current of 14.4 A. The efficiency is limited by the wavelength nonuniformity of the pump array, which reduces the absorbed power, and by the power nonuniformity, which causes some of the microchip lasers to operate near threshold where they are less efficient. Individual microchip lasers, whose pump wavelengths have been optimally tuned, have demonstrated optical efficiencies of 40%. We expect that with a full operational 1-cm² diode pump array (60 diode elements and a total CW power of 48 W at 809 nm) the microchip array should produce more than 20 W.

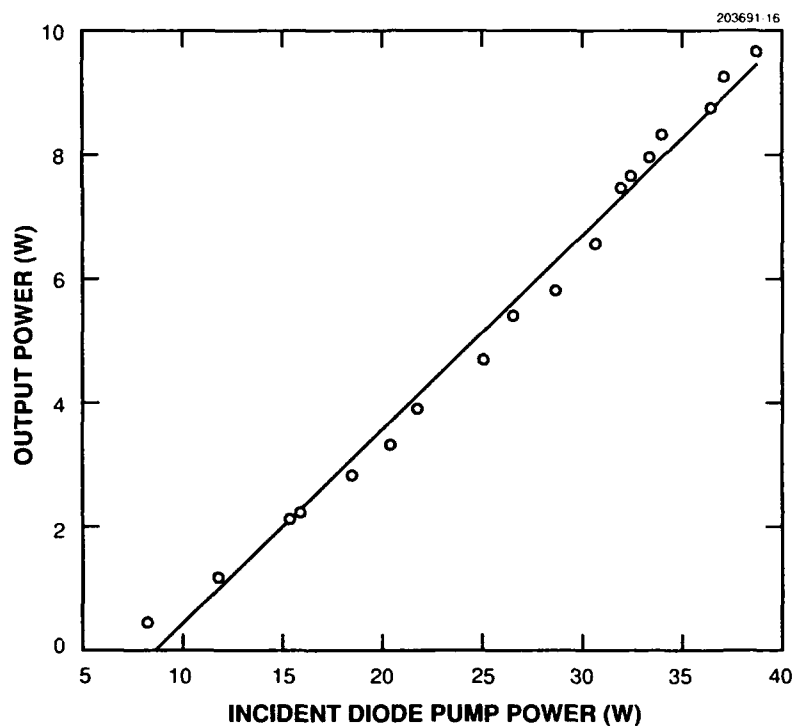


Figure 2-3. Output power from the Nd:YAG laser array as a function of incident pump power. Diode laser temperature is varied to maximize Nd:YAG laser output.

The ensemble far-field divergence of the microchip array has been compared to the calculated divergence from a single element and has been found to be nearly diffraction limited. This result indicates not only that the beam quality of the individual elements is good, but that the parallelism of the beams must be much less than the diffraction-limited divergence of a single-element beam.

C. D. Nabors
A. Sanchez-Rubio
A. Mooradian

2.3 FREQUENCY-MODULATED MICROWAVE SOURCE USING BEATS BETWEEN ORTHOGONAL MODES OF A SINGLE LASER

Microwave radiation can be generated with lasers at frequencies limited by the bandwidth of the photodetector. Recent progress in photodetectors has extended bandwidths to 60 GHz in commercial products and to 375 GHz in research devices [9], suggesting that laser driven sources of millimeter and submillimeter waves will be possible in the near future. Limitations of current solid state laser microwave sources include the need for two lasers and the inability to modulate the microwave frequency beyond tens of kilohertz. Here, we describe a new technique that generates frequency-modulated microwaves using a single laser.

When a single laser generates two optical frequencies, small length changes of the cavity (e.g., small mirror motions resulting from vibration) pull both optical frequencies in the same direction. Because of this, the microwave frequency generated in a photomixer from a two-frequency laser is much more stable than that from two single-frequency lasers. For example, typical frequency jitter of a free-running laser is 1 MHz, which causes 1.4-MHz frequency jitter in the microwave if two independent lasers are used. With a single laser generating both frequencies, a 30-GHz microwave source with ~ 100 -Hz frequency stability is possible in free-running operation.

A schematic of the laser setup is shown in Figure 2-4(a). A 0.5-W AlGaAs diode laser at 808 nm pumps the Nd:YAG laser and is isolated from it by a linear polarizer and quarter-wave plate. The dichroic mirror of 50-cm radius of curvature transmits 808 nm but is highly reflecting at 1064 nm. The 3-mm-long Nd:YAG crystal is placed near the center of the laser cavity so that spatial hole burning will tend to make two adjacent longitudinal modes operate. The 3-mm-long LiTaO₃ crystal has gold electrodes on the two faces whose normal is along the optic axis of the crystal (Z axis) and between which a microwave signal is applied, antireflection coatings on the two faces whose normal is along the direction of optical propagation (X axis), and acoustic damping on the four faces whose normals are along the Y and Z axes. The end mirror has a 5-cm radius of curvature and 95% reflectivity at 1064 nm. Proper orientation of the birefringent LiTaO₃ allows the two orthogonal polarizations to overlap in the cavity and have equal round-trip losses.

In order to tune the microwave frequency, it is necessary that the change in optical cavity length be different for the two polarizations. Figure 2-4(b) shows the optical frequencies emitted from the diode-pumped Nd:YAG laser as measured with a scanning Fabry-Perot spectrum analyzer. The anisotropy of LiTaO₃ causes the frequency of the vertically polarized light to be sensitive to voltage, while the frequency of the horizontally polarized light is insensitive to voltage. The spectrum of the vertically polarized light shifts by ~ 2 GHz when 400 V is applied. The spectrum of the horizontally polarized light does not shift noticeably on this frequency scale. The voltage tuning of the microwave frequency over nearly an octave is shown in Figure 2-5.

Using stress applied to a monolithic Nd:YAG laser, Owyong and Esherick [10] tuned a two-frequency laser over a few gigahertz with a short-term (~ 1 ms) stability of 30 kHz. Several problems were apparent: (1) instabilities caused the relaxation oscillation sidebands to be down by only 10 dB from the heterodyne signal, (2) the microwave frequency tuning speed was limited by the stress tuning technique, and (3) sometimes the two-frequency laser would lase on modes separated by several angstroms (~ 1 THz).

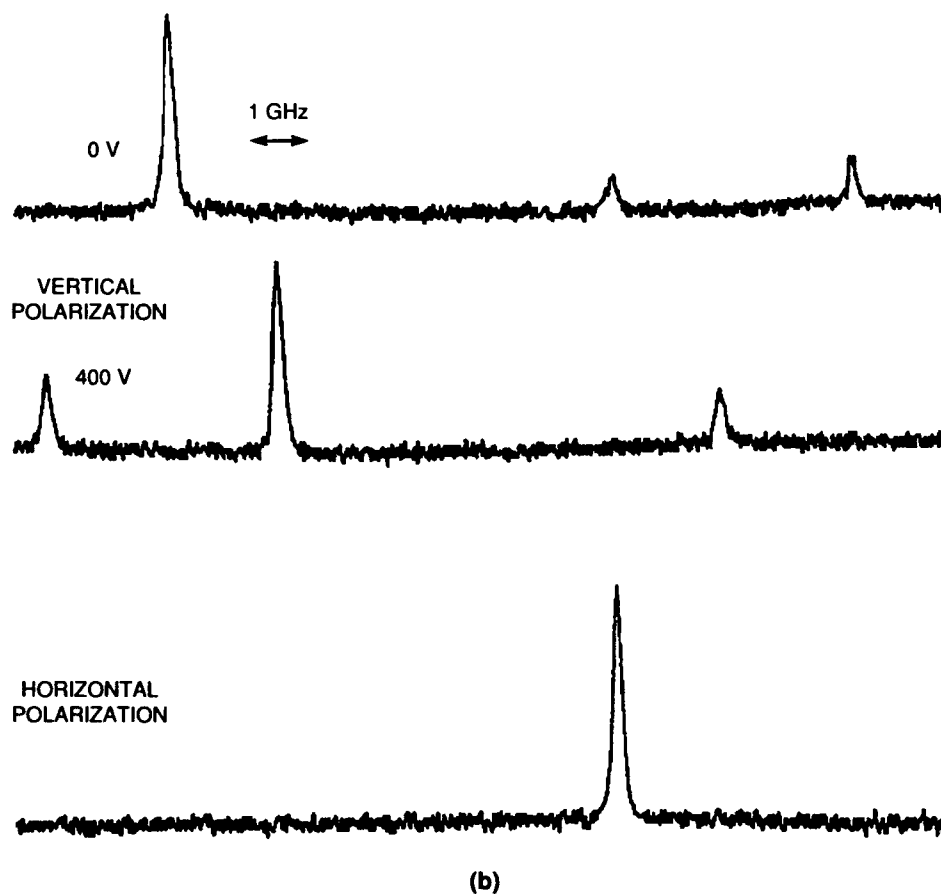
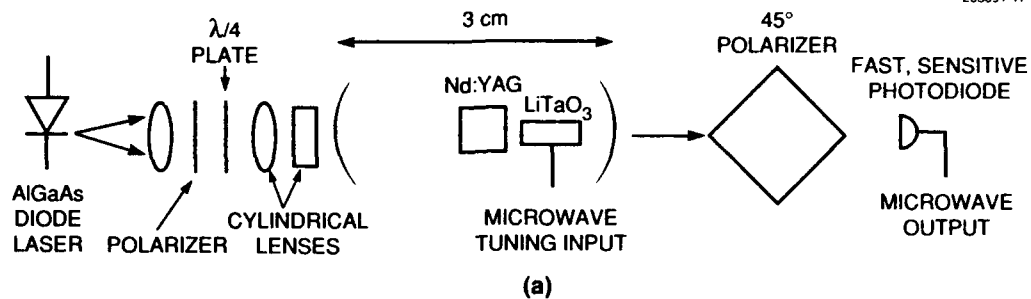


Figure 2-4. (a) Schematic of the laser-generated frequency-modulated microwave source. A single Nd:YAG laser is operated simultaneously in two polarizations. To generate microwaves, the output is passed through a polarizer oriented at 45° so that the difference frequency can be generated in a fast photomixer. (b) Fabry-Perot spectra of the laser output in vertical and horizontal polarizations. The top two spectra show that the laser has predominantly one vertically polarized mode but with two other weaker modes also apparent; the frequency shifts at ~ 5 MHz/V. The bottom spectrum shows that the laser operates in only one mode of horizontal polarization; the frequency does not change with applied voltage.

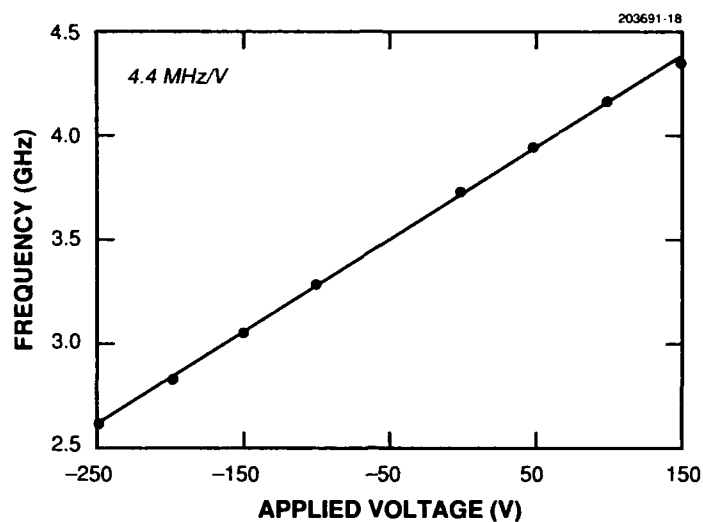


Figure 2-5. Tuning of the microwave frequency. The microwave signal tuned with voltage with a sensitivity of 4.4 MHz/V.

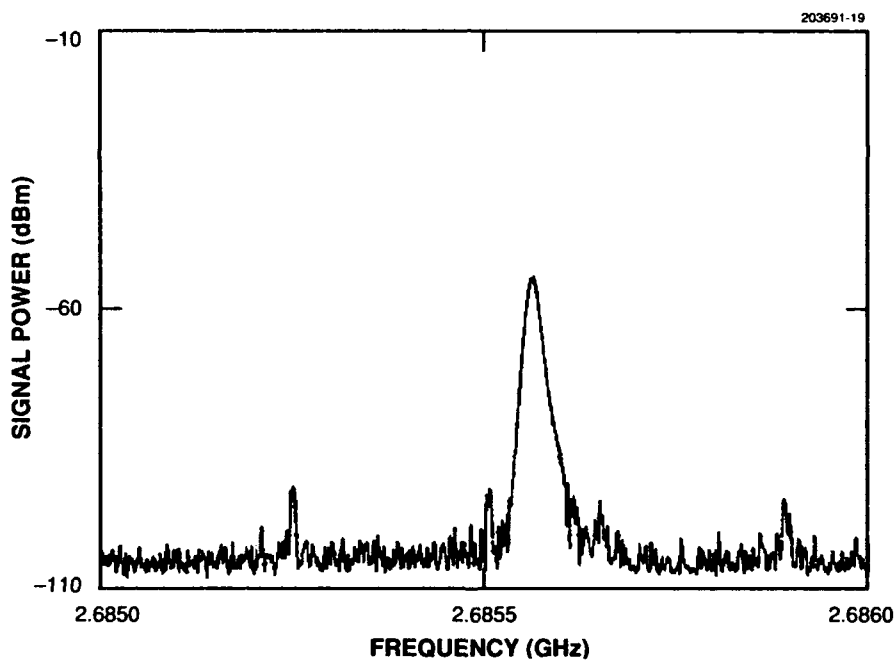


Figure 2-6. Microwave spectrum of the photomixer. The microwave intensity is -54 dBm and is limited by the amount of optical power that can be dissipated in the photomixer. The relaxation oscillation sidebands that are 320 kHz from the main peak are suppressed by 40 dB from the principal microwave beat note.

The laser we have built has eliminated these three problems while improving the short- and long-term stability. Figure 2-6 shows the microwave spectrum, which indicates that the relaxation oscillation is lower than the heterodyne signal by 40 dB. This relaxation oscillation is 3 orders of magnitude weaker than that reported in [10] and may be the result of a more stable cavity, of less feedback to the pump diode laser, and of more stable mode intensities since spatial hole burning occurs. The short-term (1 ms) frequency stability is 3 kHz.

The microwave tuning speed is higher using the electrooptic effect rather than the piezoelectric (stress) effect. Voltages for tuning in the frequency range from dc to 250 MHz gave uniform electrooptic response [11]. The modulation bandwidth of 250 MHz was limited by the electronic circuit and could be made significantly wider with a different high-frequency circuit. Indeed, in a single-frequency laser, good electrooptic response out to 5 GHz has been obtained using an alternative circuit.

The specific location of the laser crystal within the cavity determines the frequencies of the two orthogonally polarized modes. Selecting the modes in this way stabilizes the individual mode intensities, which reduces the amplitude of relaxation oscillations and provides more stable microwave frequencies.

S. R. Henion

P. A. Schulz

REFERENCES

1. J. J. Zayhowski, J. L. Daneu, C. Cook, C. Dill, and R. C. Hancock, Solid State Research Report, Lincoln Laboratory, MIT, 1991:4, p. 14.
2. J. J. Zayhowski and A. Mooradian, *Opt. Lett.* **14**, 24 (1989); **14**, 618 (1989).
3. J. J. Zayhowski and P. L. Kelley, *IEEE J. Quantum Electron.* **27**, 2220 (1991).
4. G. Winzer, P. G. Möckel, R. Oberbacher, and L. Vité, *Appl. Phys.* **11**, 121 (1976).
5. G. Huber, in *Current Topics in Materials Science*, E. Kaldis, ed., Vol. 4. (North-Holland, Amsterdam, 1980), p. 1.
6. M. E. Storm, *OSA Proc. Advanced Solid-State Lasers* **6**, 140 (1991).
7. T. Taira, A. Mukai, Y. Nozawa, and T. Kobayashi, *Opt. Lett.* **16**, 1955 (1991).
8. J. J. Zayhowski, *Opt. Lett.* **16**, 575 (1991); and erratum, *Opt. Lett.* **16**, 1287 (1991).
9. F. W. Smith, H. Q. Le, V. Diadiuk, M. A. Hollis, A. R. Calawa, S. Gupta, M. Frankel, D. R. Dykarr, G. A. Mourou, and T. Y. Hsiang, *Appl. Phys. Lett.* **54**, 890 (1989).
10. A. Owyong and P. Esherick, *Opt. Lett.* **12**, 999 (1987).
11. S. R. Henion and P. A. Schulz, *Opt. Lett.* **16**, 578 (1991).

3. MATERIALS RESEARCH

3.1 MEASUREMENT OF RHEED OSCILLATIONS DURING MBE GROWTH OF GaAs ON A ROTATING SUBSTRATE

Analysis of reflection high-energy electron diffraction (RHEED) intensity oscillations is one of the most useful in situ techniques for the measurement and control of molecular beam epitaxy (MBE) growth of a variety of materials [1],[2]. Recently, the use of frequency-domain techniques has made it possible not only to achieve a better understanding of well-resolved RHEED oscillations [3], but also to obtain oscillation data for growth under conditions that make the conventional time-domain methods difficult or impossible to apply [4],[5]. However, a major limitation of all previous RHEED oscillation analysis methods is that substrate rotation, which is generally employed in order to improve uniformity of the growing films and interfaces, must be stopped in order to obtain a fixed diffraction pattern from which oscillation data can be obtained. We have now developed a technique that permits the acquisition of RHEED oscillation data while the substrate continues to rotate, and we have used this technique in experiments on the MBE growth of GaAs. The capability of performing RHEED analysis on rotating substrates could lead to improvements in the quality of complex epitaxial structures and interfaces for which interrupting rotation can have a deleterious effect.

A commercial 3-in. MBE system was used for GaAs growth. The GaAs substrates were chemically cleaned and etched, mounted with In on Mo blocks, and heated in the growth chamber to accomplish oxide desorption. Typical growth conditions were employed, including an As_4/Ga beam-equivalent pressure of ~ 10 , a growth rate of $\sim 1 \mu\text{m/h}$, and a substrate temperature of $\sim 600^\circ\text{C}$.

A schematic diagram of the measurement system is shown in Figure 3-1. The RHEED image is generated by a conventional RHEED gun operated at 8 kV, with the diffracted beam incident on a phosphor screen. The image on the screen is captured with a video system consisting of a charge-coupled device TV camera with RS-170 video output, a 16-MHz 80386-based desktop computer with an 8-bit 640×480 -pixel frame grabber board, and a TV monitor. The frame grabber board can acquire an entire image in $1/30$ s, a capture rate that yields a flicker-free display of the image on the monitor. No synchronization is required between the substrate rotational drive and the computerized video tracking system, so a RHEED oscillation measurement can be initiated at any azimuth of substrate rotation, and a standard video tape recorder can be used to store RHEED intensity data for subsequent analysis.

A significant task in developing the video analysis system was to devise a method for extracting useful RHEED oscillation data from the video images captured by the frame grabber. Initially, it was hoped that identifying and then tracking the diffracted intensity patterns associated with a specified set of azimuths would make it possible to collect the needed oscillation information from selected points on these patterns as they swept across the phosphor screen during substrate rotation. At normal rotation speeds, however, the intervals during which no identified pattern was present on the screen were too great to permit satisfactory analysis. Fortunately, it was found that tracking the region of diffracted intensity

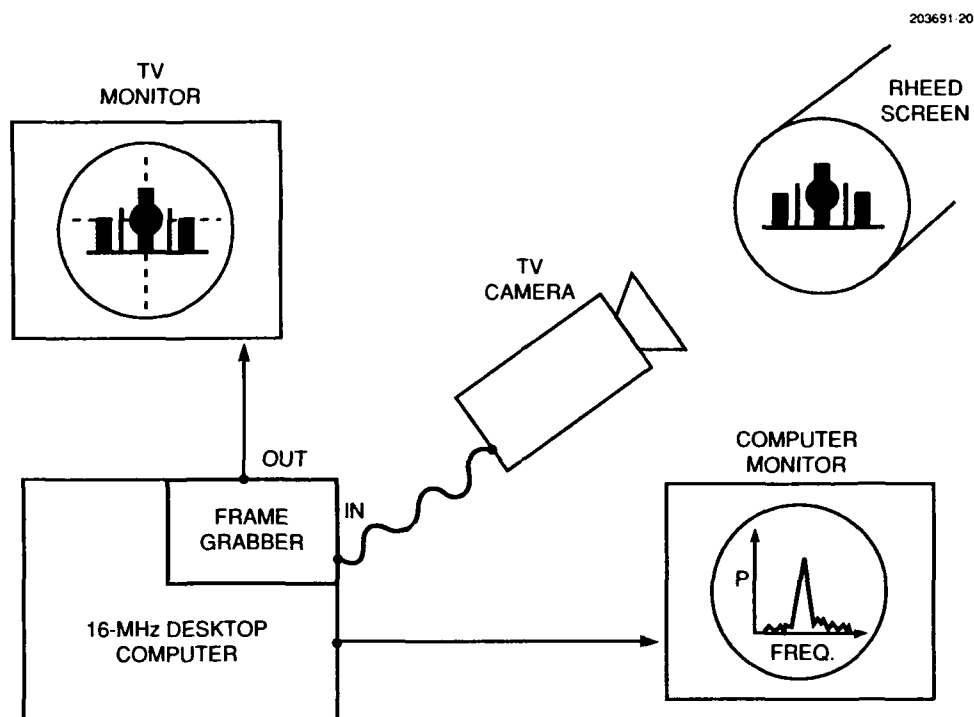


Figure 3-1. Schematic of video tracking and data analysis system.

generated by the specular reflection of the electron beam from the substrate surface permits useful RHEED oscillation information to be extracted from the video data.

To track the region of specular reflection we tried three approaches. A single-pixel tracking method was quickly abandoned because of the magnitude of the movement of the reflected beam due to nonplanar bonding of the substrate, instabilities in the electron gun, and wobble in the mechanical components of the azimuthal rotation apparatus. In addition, the spatial extent of the image of the reflected beam, together with the limited dynamic range of the frame grabber board, made evaluation of the peak intensity difficult. As a second approach, from the full video image we selected a rectangular subframe that included the entire specular reflection, and the reflection was tracked by moving this subframe. However, the computational overhead required to analyze the intensity data associated with the large numbers of pixels contained in the subframe was so high that the processing rate dropped to ~ 5 frames/s. This rate was too low to give enough data for accurately determining the oscillation frequency for growth at our normal rotation rate of 10 rpm. In the successful approach, we selected a combination of 64 pixels in a single horizontal row and 64 pixels in a single intersecting vertical column to track the region of specular reflection. With these two lines of pixels, the position of the peak intensity of the specular reflection could be accurately tracked.

Because of the limited dynamic range of the frame grabber board, it is necessary to be able to evaluate the peak intensity from data for lines of pixels of which one or more can have a saturated intensity value. This task has been accomplished by fitting the intensity profile to a Gaussian function and then estimating the peak intensity in the absence of saturation. With the combination of tracking and intensity analysis, we are able to process video data at up to ~ 20 frames/s. This rate yields an uncertainty of $\sim 1\%$ in a growth rate of $1\text{ }\mu\text{m/h}$.

The intensity data extracted from the video system are analyzed by means of frequency-domain techniques described previously [4]. For the rotational RHEED data, digital filtering must be performed to remove spurious frequency components. A relatively wide bandpass filter, with a $\pm 20\%$ frequency cutoff, was found adequate for this purpose. At present, the analysis is performed after all the data have been collected. With improved computer hardware it should be possible to analyze the data in real time.

Figure 3-2 shows the power spectrum obtained by frequency-domain analysis of data for a nonrotating GaAs sample that were taken with the video tracking system operating at ~ 20 frames/s, with a well-resolved peak at 1.17 Hz. The time-domain data taken for the same sample at a rotation rate of 5 rpm are represented in Figure 3-3. No oscillatory behavior is apparent. Figure 3-4 shows the power spectrum of the data from Figure 3-3, with a peak at 1.15 Hz. The power spectrum obtained by frequency-domain analysis of data taken for the same sample rotating at 10 rpm demonstrates a well-resolved central peak of 1.17 Hz. Thus, for static, 5-rpm, and 10-rpm experiments, the extracted frequencies agree to within 2%.

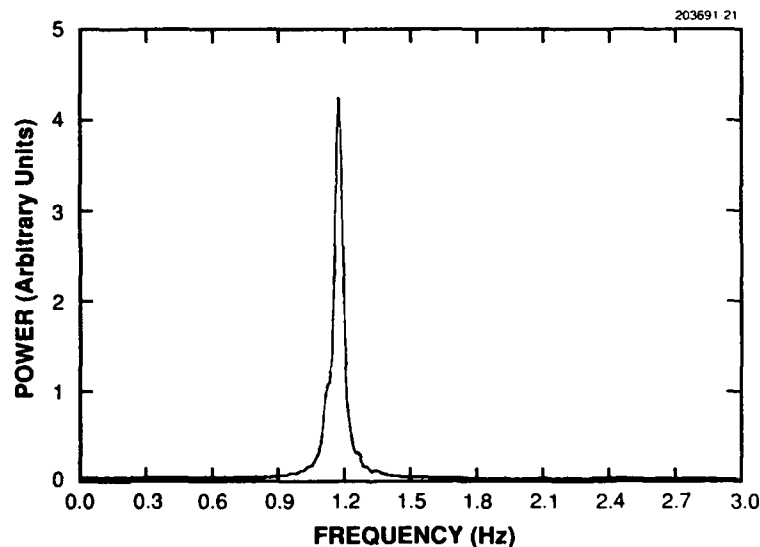


Figure 3-2. Power spectrum of RHEED intensity data for a nonrotating GaAs sample.

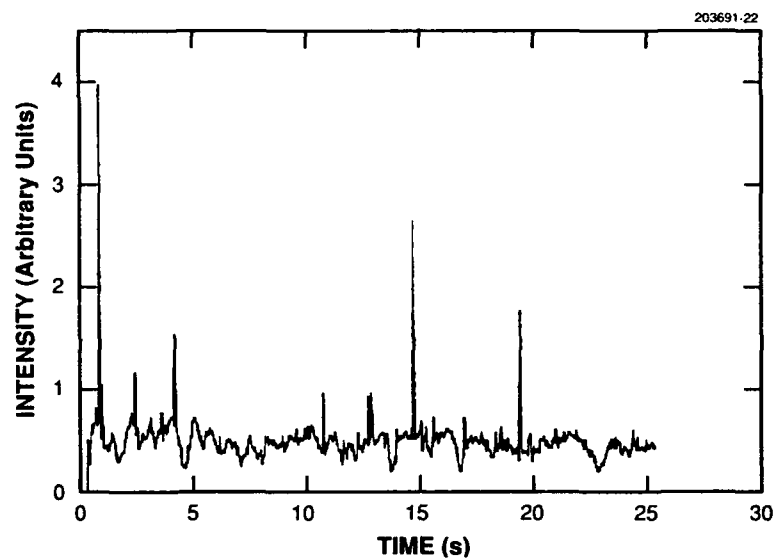


Figure 3-3. RHEED intensity data for the same sample as in Figure 3-2 taken at a rotation rate of 5 rpm.

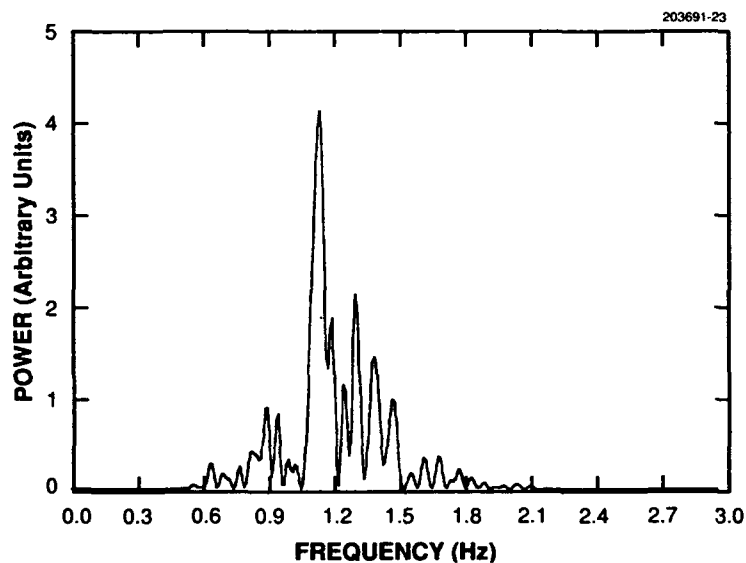


Figure 3-4. Power spectrum of data from Figure 3-3.

It has previously been reported [6] that phase relationships of RHEED oscillations as a function of azimuthal angle for GaAs growth are quite complex because of the interaction of multiple scattering processes. It is somewhat surprising, therefore, that sufficient signal power of the fundamental oscillation

frequency can be recovered to permit discrimination of this frequency from the other components that are present. The details of the discrimination process should be investigated further.

G. W. Turner
A. J. Isles*

3.2 TIME AND TEMPERATURE DEPENDENCE OF PHOSPHORUS VAPOR PRESSURE

The vapor pressure values provided by some current suppliers of red P differ considerably from those reported in the most recent study of the vapor pressure of red P, which was done by Bachmann and Buehler in 1974 [7]. Furthermore, violent explosions have occurred during the synthesis of InP in sealed fused silica ampoules even when the suppliers' data were used to estimate the P vapor pressure. To avoid such explosions, we have developed a technique for accurately balancing the P pressure inside the sealed synthesis ampoule with high-pressure Ar gas in a steel pressure vessel [8]. We have recently utilized the pressure balancing apparatus and technique to investigate the time and temperature dependence of P vapor pressure.

For each run, a fused silica ampoule is loaded with red P, evacuated to 10^{-6} Torr, and sealed. The ampoule is then inserted into a hollow copper cylinder, and this assembly is placed in a resistance-heated tube furnace inside the steel pressure vessel, which can be pressurized with Ar gas up to 40 atm. Figure 3-5 is a schematic cross-sectional diagram of the apparatus. A fused silica diaphragm is incorporated at one end of the silica ampoule to sense the difference between the pressures inside and outside the ampoule, and two fused silica arms are attached to the diaphragm. As the diaphragm flexes, the distance between the arms changes. A voltage V that depends on this distance and therefore on the differential pressure is generated by means of two linear variable differential transformers (LVDTs), one mounted at the end of each arm.

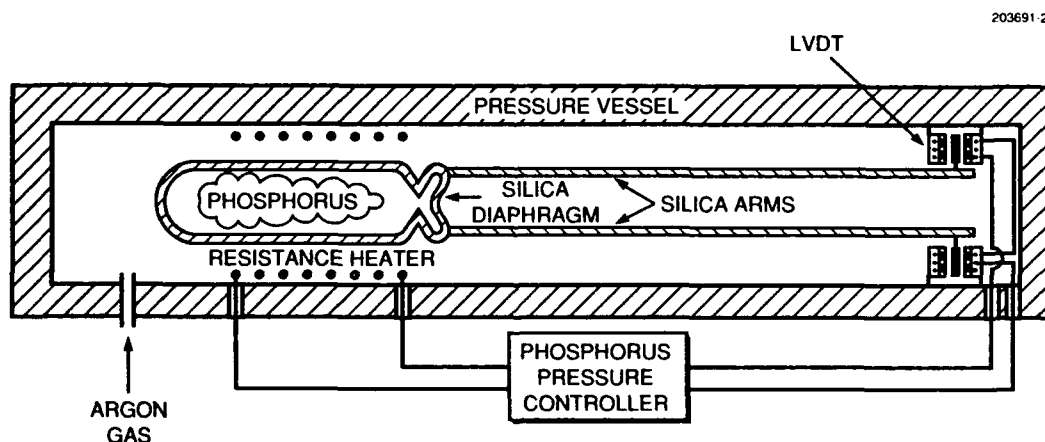


Figure 3-5. Schematic diagram of apparatus for measuring phosphorus pressure.

At the beginning of a run, with the ampoule evacuated and the pressure vessel filled with air at 1 atm, the value of V , designated V_1 , corresponds to a differential pressure of 1 atm. The pressure vessel is then evacuated. The new value of V , designated V_0 , is the pressure-balanced value. The sensitivity of the transducer is thus

*Author not at Lincoln Laboratory.

($V_1 - V_0$) per atmosphere of differential pressure. The measured sensitivity has ranged from 2 to 10 V/atm. To initiate a measurement run, the furnace is slowly heated to begin generating P_4 vapor, and Ar is admitted to the pressure vessel under manual control to balance the P pressure. To perform a P' pressure measurement, the Ar pressure is adjusted to make V equal to V_0 , so that the P pressure is given by the Ar pressure.

Data obtained in heating runs on P samples from three suppliers are shown in Figure 3-6, where the measured P pressure is plotted on a logarithmic scale as a function of reciprocal absolute temperature. The samples of materials 1 and 3 consisted of a number of millimeter-sized chunks, while the sample of material 2 was a single chunk weighing about 25 g. The heating curve for material 1 lies well below even the lowest pressure-temperature curve reported by Bachmann and Buehler [7]. It is likely that the heating rates for this material, which varied from $\sim 7^\circ\text{C}/\text{min}$ at 400°C to $\sim 1^\circ\text{C}/\text{min}$ at 500°C , were too rapid for sublimation to raise the P pressure to the equilibrium values. The pressure values for material 2 are even lower than those for material 1. Since the heating rates for material 2 were somewhat lower than those for material 1, the observation of lower pressures for material 2 probably resulted because the sample was a single large chunk that had lower sublimation rates because of its smaller surface area.

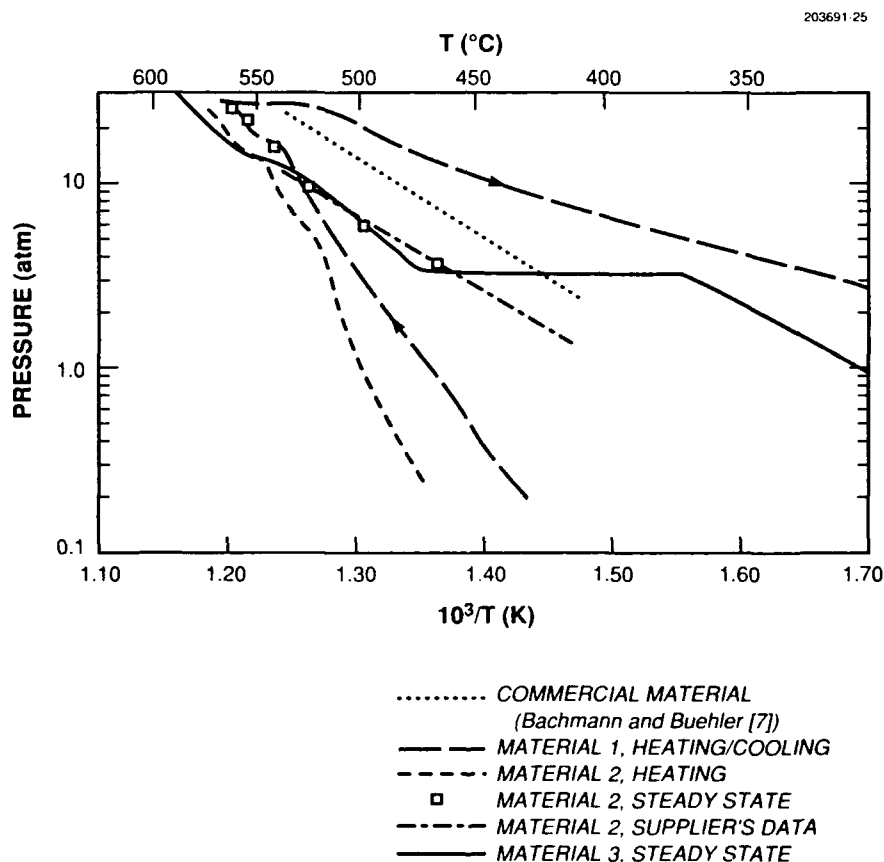


Figure 3-6. Phosphorus pressures measured during heating and cooling vs reciprocal absolute temperature.

In a series of experiments to investigate the sublimation rate of red P more directly, a cube of material 2, measuring 2.2 cm on a side, was sealed into a 150-cm³ ampoule. The temperature was first raised as rapidly as possible to 460°C and then held constant until the P pressure became constant. More than an hour was required for the pressure to reach 90% of its final value. The rate of pressure increase between 1 and 2 atm corresponds to sublimation of about 4×10^{17} atoms cm⁻² s⁻¹ at this temperature. Similar experiments were then performed at five additional temperatures up to 560°C. Even at the highest temperature, the time required to reach the final pressure was more than 30 min. The final pressures measured at the six temperatures are plotted in Figure 3-6. The three lower temperature points agree quite well with the data provided by the supplier of this material, but the points at 540°C and above lie significantly higher. The pressure curve of Bachmann and Buehler [7] for commercial amorphous red P lies about a factor of 2 higher than that for the data provided by the supplier of material 2 in 1991.

In a second experiment to estimate the rate of sublimation, a second cube of material 2 about 1.8 cm on a side was sealed into another ampoule. In this case the temperature was raised as rapidly as possible to 540°C and then held constant. The measured pressure vs time is plotted in Figure 3-7. The rate of pressure increase from 4 to 6 atm corresponds to sublimation of about 2×10^{18} atoms cm⁻² s⁻¹.

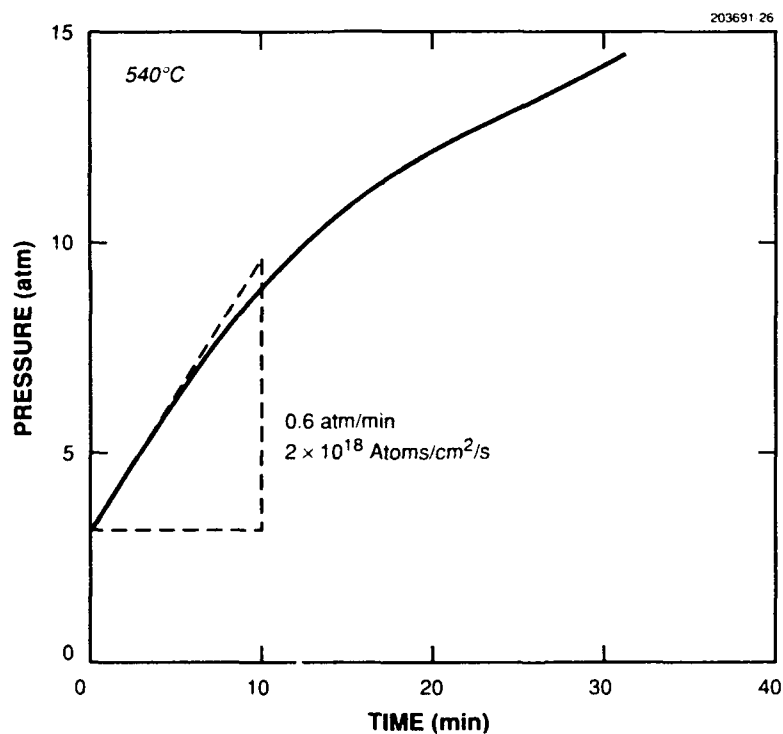


Figure 3-7. Phosphorus pressure vs time at constant temperature.

Data nearly identical to the cooling curve obtained for material 1 were reported for liquid white P by Smits and Bokhorst in 1916 [9]. It is well known that liquid white P melts at 44°C and consists of tetrahedral P₄ molecules weakly bonded by van der Waals forces. It is also known that P vapor in a closed system in the temperature range of our measurements consists almost entirely of P₄ molecules. From this information, together with the cooling curve for material 1, it is apparent that the stable P₄ molecule in the vapor phase can rapidly condense only on white P, not on either solid red P or the fused silica ampoule walls. When a closed ampoule containing only solid red P and its vapor is cooled, the pressure therefore does not decrease (except by the gas law) until the temperature reaches the equilibrium curve for white P.

The heating curve for material 3 exhibits an unexpectedly large and nearly constant pressure between 370 and 460°C. We propose that this material contained some white P, and that by the time the temperature reached 370°C either the white phase had converted to red or the total quantity of white P had evaporated. In either case the pressure would not be expected to increase further (except by the gas law) until the temperature had reached the equilibrium red P vapor pressure curve, nor would it be expected to decrease since no solid white P was present to permit rapid condensation.

The heating and cooling experiments demonstrate that the sublimation, condensation, and condensed-phase transformation of P are subject to severe kinetic limitations. Because of these limitations, the P pressure during InP synthesis in sealed ampoules can deviate greatly from the equilibrium pressure of amorphous red P at the reservoir temperature. We believe that explosions occurring during synthesis are primarily caused by deviations from equilibrium, not by sample-to-sample differences in the equilibrium vapor pressure. The pressure-balanced synthesis technique overcomes problems due to such deviations.

G. W. Iseler
H. R. Clark, Jr.
D. F. Bliss*

*Author not at Lincoln Laboratory.

REFERENCES

1. T. Sakamoto, K. Sakamoto, S. Nagao, G. Hashiguchi, K. Kuniyoshi, and Y. Bando, *Thin Film Growth Techniques for Low-Dimensional Structures* (Plenum, New York, 1986), p. 225.
2. P. J. Dobson, B. A. Joyce, J. H. Neave, and J. Zhang, *J. Cryst. Growth* **81**, 1 (1987).
3. B. A. Joyce, J. Zhang, J. H. Neave, and P. J. Dobson, *Appl. Phys. A* **45**, 255 (1988).
4. G. W. Turner, B. A. Nechay, and S. J. Eglash, *J. Vac. Sci. Technol. B* **8**, 283 (1990).
5. J. Kraus, J. Weyers, W. Prost, and F. J. Tegude, *Conf. Proc. Euro MBE 1991* (Tampere University of Technology, Finland, 1991), p. Cp2.
6. J. Zhang, J. H. Neave, P. J. Dobson, and B. A. Joyce, *Appl. Phys. A* **42**, 317 (1987).
7. K. J. Bachmann and E. Buehler, *J. Electrochem. Soc.* **121**, 835 (1974).
8. G. W. Iseler and H. R. Clark, Jr., *Proc. 2nd Int. Conf. on InP and Related Materials* (IEEE, New York, 1990), p. 25.
9. A. Smits and S. C. Bokhorst, *Z. Phys. Chem.* **91**, 249 (1916).

4. SUBMICROMETER TECHNOLOGY

4.1 LASER-INDUCED DAMAGE IN PELLICLES AT 193 nm

The drive toward continually smaller features in semiconductor device fabrication has presented ever more demanding challenges to photolithography. In response, photolithographic techniques have expanded to include high-numerical-aperture projection optics, phase shifting masks, innovative illumination schemes, and a gradual shift to shorter wavelengths. Although the theoretical scaling of resolution with wavelength favors a shift to 193 nm, several key issues need to be addressed before 193-nm lithography is considered a practical technology. One of these issues is the long-term stability of the various optical components upon prolonged irradiation with 193-nm photons. The combination of high photon energy (6.4 eV) and the pulsed nature of the laser (which implies high peak powers) may cause gradual changes to nominally transparent optical materials [1], optical coatings, and pellicles.

Here, we report on studies of 193-nm-induced damage to pellicles currently designed for 248-nm use. We have exposed pellicles from DuPont and Exion, both materials having proprietary formulations. Since the DuPont pellicles are based on a modified version of Teflon AF 1600, we have also performed studies on thin films of Teflon AF 1600 spun on substrates of UV-grade fused silica. In all instances radiation-induced changes were observed, with the pellicles ultimately being completely ruptured. A quantitative analysis of these effects shows a nonlinear dependence on laser fluence, and this dependence was used to estimate the useful lifetime of the pellicles in a 193-nm production environment.

In our experiments the 193-nm exposures were performed using a commercial laser at 150-Hz pulse repetition rate and with pulses of 23 ns full width at half-maximum. Most of the exposures were performed in air, after we determined that the rate of degradation did not change when the ambient was dry nitrogen. Transmission spectra in the range 190–820 nm were taken at regular intervals, and the resulting interference pattern was used to calculate the product of thickness and refractive index of the pellicle. The contrast of the initial spectrum was used to calculate the index of refraction in the 500–800-nm region (1.31) and hence the pellicle thickness. Although subsequent spectra showed reduced contrast, this change was attributed to surface roughening due to inhomogeneities in laser intensity rather than to a decrease in index of refraction. Confirmation was obtained from mechanical stylus profilometer scans on the Teflon AF 1600 thin films on fused silica substrates. The average thickness obtained with stylus profilometry agreed with that measured optically, indicating that the index was practically unaltered by the laser exposure. The transmission spectra of the pellicles and thin films were therefore used to calculate the respective thicknesses, using the constant-index approximation.

Figure 4-1 shows the evolution of the thickness of DuPont and Exion pellicles with increasing dose at the fixed fluence of $5 \text{ mJ cm}^{-2}/\text{pulse}$. The two pellicles have different initial thicknesses, and they probably differ also in chemical composition, but their behavior is quite similar: in the first stage the thickness changes little, then the pellicle is gradually thinned at a rate approximately linear with the cumulative dose, and finally it ruptures completely. This behavior at 193 nm should be contrasted with no observable changes at 248 nm ($1 \text{ mJ cm}^{-2}/\text{pulse}$, 10^7 pulses) [2]. The number of laser pulses required to rupture the pellicle is a convenient indicator of the laser-induced damage. In Figure 4-2 this number

vs the laser fluence is plotted (on a log-log scale) for pellicles from DuPont and Exion with the initial thicknesses indicated. The number of pulses required to rupture is inversely proportional to a power of the fluence, the value of this power being ~ 1.7 . It should be noted that our exposures were performed at the relatively high fluence of $4 \text{ mJ cm}^{-2}/\text{pulse}$. In a commercial stepper or step-and-scan system the fluence at the pellicle is expected to be much smaller. In fact, if the fluence at the wafer is $\sim 1 \text{ mJ cm}^{-2}/\text{pulse}$, a $4\times$ reduction system with 50% transmission would imply $0.125 \text{ mJ cm}^{-2}/\text{pulse}$ at the mask and pellicle. Extrapolation of our results to those fluences indicates that rupture of the pellicle would take place after 10^{10} – 10^{11} pulses. This number of pulses corresponds to more than 10 years of full-time operation in a semiconductor production environment.

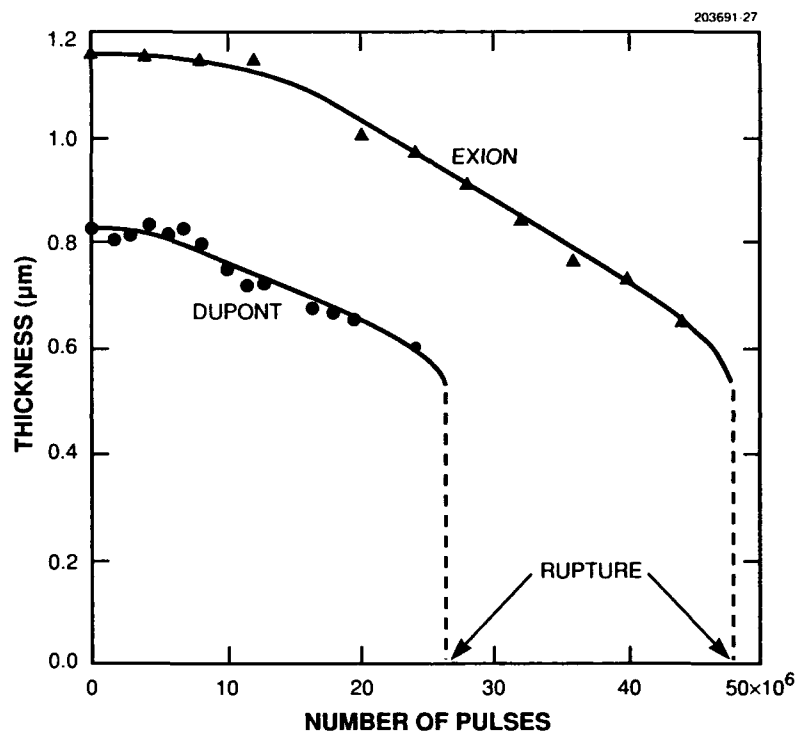


Figure 4-1. Change in thickness of a DuPont and an Exion pellicle, exposed at 193 nm at a fluence of $5 \text{ mJ cm}^{-2}/\text{pulse}$.

The 193-nm-induced degradation of the pellicle material is apparently a photochemical bond scission process, in which oligomers of successively smaller length are formed and eventually volatile products are generated. Since removal of oxygen from the ambient does not affect the rate of thinning, the photochemical reaction is intrinsic to the molecular system. The power dependence of 1.7 in Figure 4-2 indicates that the coupling of laser power into the material is a combination of one-photon absorption, which would have a power dependence of 1.0, and two-photon absorption with a respective dependence

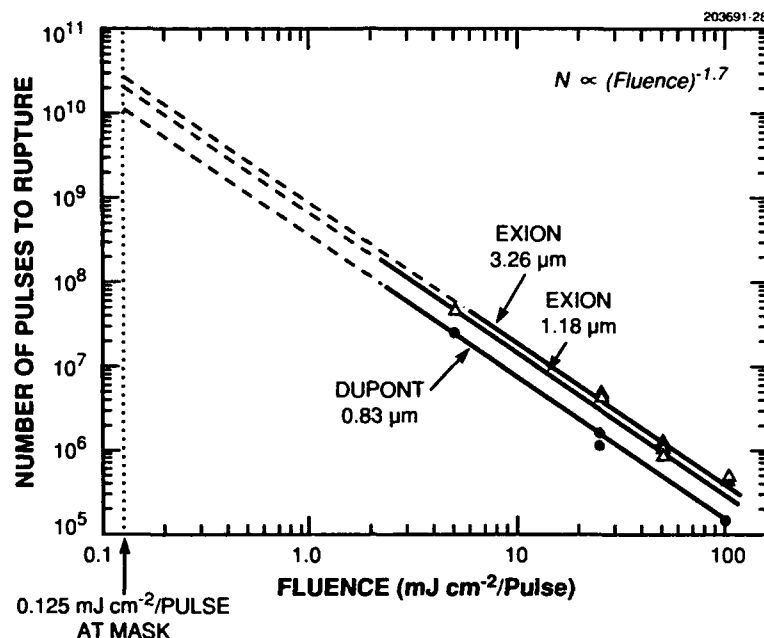


Figure 4-2. Logarithmic plot of the number of 193-nm pulses required to rupture a pellicle, for several fluences in the range 4 to 100 $\text{mJ cm}^{-2}/\text{pulse}$. The pellicles tested were from DuPont (initial thickness 0.83 μm) and Exion (initial thicknesses 1.18 and 3.26 μm). At the fluences expected at the mask in a stepper ($\sim 0.1 \text{ mJ cm}^{-2}/\text{pulse}$), the pellicles would rupture in 10^{10} – 10^{11} pulses.

of 2.0. Indeed, the DuPont pellicle exhibits a small amount of absorption (~ 1 – 2%) at wavelengths below $\sim 200 \text{ nm}$, and the same is true of the Exion pellicles. Therefore, one-photon absorption may contribute to the laser-induced damage at 193 nm, although a two-photon process plays a critical role as well.

The DuPont pellicles are made of material related to Teflon AF 1600, but the pellicle material has a lower molecular weight ($\sim 220\,000$ in the pellicle vs $\sim 465\,000$ for Teflon AF 1600) and a lower glass transition temperature [3]. The nature and distribution of polymeric end groups may also be different. Keeping these differences in mind, we have performed a series of exposure studies on thin films of Teflon AF 1600 spun on transparent fused silica substrates. The thicknesses of these films are in the range 0.2–2.2 μm . They do not show absorption at 193 nm. Nevertheless, they are thinned by laser irradiation in much the same way as the pellicles. The thinning rate is proportional to the film thickness, and as Figure 4-3 demonstrates, the evolution of the normalized thickness exhibits an exponential behavior with increasing number of pulses, with the exponential coefficient varying with fluence. The dependence of this coefficient on fluence is approximately quadratic, indicating a predominantly two-photon absorption process. The radiation-induced damage in the DuPont and Exion pellicles proceeds ~ 10 times faster (at a fixed fluence) than that in Teflon AF 1600 thin films. While a factor of 2 could be expected because of the two exposed surfaces in pellicles vs the one in thin films, the extra factor of ~ 5 must be attributed to the pellicle's lower molecular weight or its small amount of one-photon absorption.

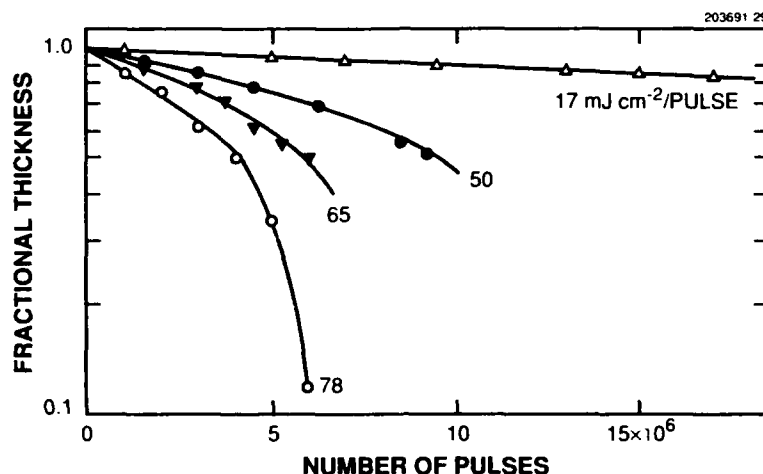


Figure 4-3. Evolution of the thickness of Teflon AF 1600 thin films on fused silica (normalized to their initial thickness) with increasing number of 193-nm pulses, for the four fluences indicated.

The pellicles that we have tested were optimized for 248-nm operation. We expect that, if required, specially optimized 193-nm pellicles with extended lifetimes can be made with relatively minor deviations from the corresponding 248-nm formulations.

M. Rothschild
J. H. C. Sedlacek

4.2 IONIC LIQUID-CHANNEL FIELD-EFFECT TRANSISTOR

A theoretical and experimental study was carried out on a new microfabricated device, an ionic liquid-channel field-effect transistor (ILCFET) [4]. The work was conducted to determine the feasibility of developing monolithic chemical analyzers for ions in solution. In these analyzers the ions are differentiated by mobility. The ILCFET provides a starting point to fabricate, understand, and model the more complex analyzers.

The ILCFET resembles a metal-oxide-semiconductor field-effect transistor (MOSFET), except that the current flowing from the source to the drain is carried in thin channels by ions of a liquid electrolyte. The gate voltage induces an electric field, transverse to the current flow, which controls the channel conductance. Unlike MOSFETs, in which the channel conductance depends on one mobile charge carrier, holes or electrons, the ILCFET channel conductance depends on the concentrations of both cations (positively charged ions) and anions (negatively charged ions).

The ILCFETs are composed of polysilicon gate electrodes, metal source and drain electrodes, and 50 capillary channels extending from the source to the drain. Each channel is 10 μm wide, 0.088 μm thick, and 300 μm long, and is defined by a shell of 50-nm-thick Si_3N_4 coated with 30-nm-thick SiO_2 . The two

insulation layers form a barrier to both ions and electrons. A transverse cross section of a channel is shown in Figure 4-4(a), and a longitudinal cross section through the center of the channel is illustrated in Figure 4-4(b). The channels are formed by etching sacrificial amorphous silicon out of the channel. Figure 4-5 shows 0.5- μm -thick channels just after the etch step. Using this technique we have achieved length-to-thickness aspect ratios of 30 000 for channel lengths of 3 mm.

We have modeled the device in steady state and in response to a step in the gate voltage. The channel conductance model assumes that the ions do not interact with the Si_3N_4 surface, that there is no fixed charge in the insulators or on the Si_3N_4 surface, and that the ions are point charges. The steady-state potential profile and distribution of ions in the channel across its thickness are determined by an

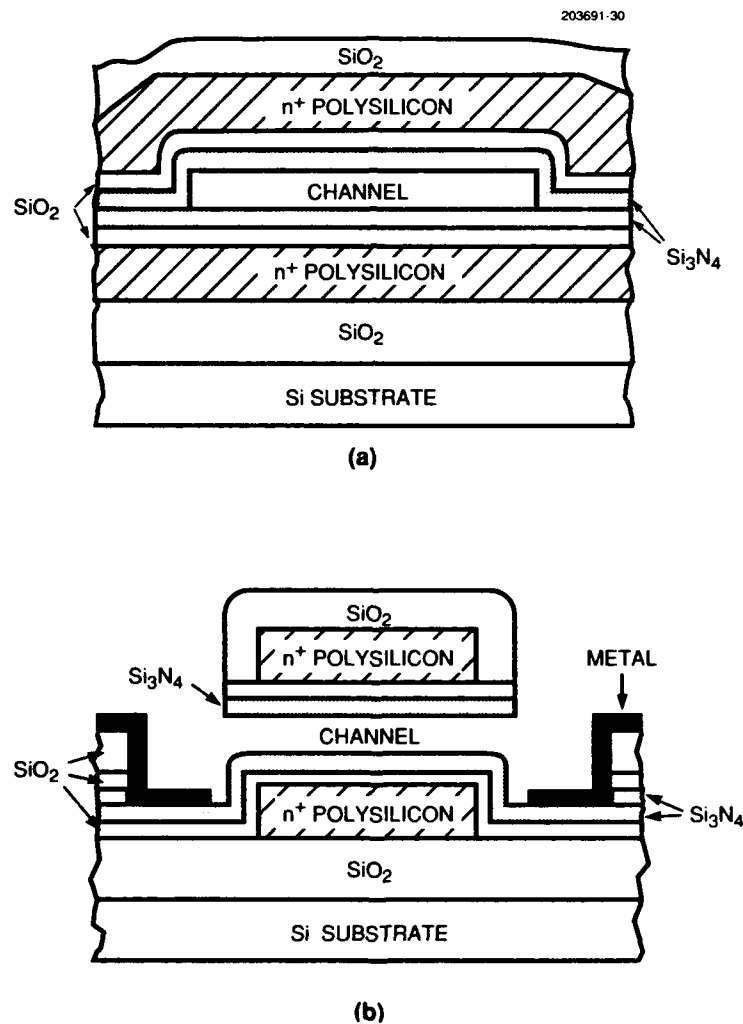


Figure 4-4. (a) Transverse and (b) longitudinal cross sections of the ILCFET (not to scale).



Figure 4-5. Scanning electron micrograph of two parallel open-air channels just after an etch of sacrificial amorphous Si. The openings to the channels are the dark areas.

approximate analytical solution to the Poisson-Boltzmann equation [5]. This solution assumes that the channel is filled with a symmetric electrolyte (one for which the charge state $|z|$ is the same for the cation and anion). With a positive bias on the gate, the majority ions are the anions. The potential profile and net charge distribution of anions over cations, symmetric about the channel center, are highest at the Si_3N_4 surface and decay toward the channel center. From the ion distributions, one predicts the steady-state channel conductance vs gate voltage curve to be an asymmetric V shape with the slope of each side proportional to the mobility of the majority ion. A theoretical steady-state channel conductance curve is shown in Figure 4-6 for an acid solution.

The transient response to a step in the gate voltage is modeled by charging of the gate capacitance followed by slower ambipolar diffusion of ion pairs until the channel reaches steady state. Both processes are described by the diffusion equation. The channel conductance will display a hysteresis effect, as illustrated in Figure 4-6, if the gate voltage is stepped before the device reaches steady state. For our devices, tested with glycerol solutions, the gate capacitance charges in about a minute. To reach steady state through ambipolar diffusion takes ~ 100 times longer than to charge the gate capacitance, so the two processes are treated as independent events.

The ILCFETs were tested with acid (1.8×10^{-3} M of H_3BO_3), base [8.9×10^{-4} M of $(\text{CH}_3)_4\text{NOH}$], and salt (5.9×10^{-4} M of KCl) solutions of glycerol in a nitrogen ambient. The gate charging current was measured as a function of time and agreed with theory. For every solution tested the slopes of the channel conductance vs gate voltage curve were typically 10–30 times less than predicted and there were ≥ 20 -V shifts in the conductance curves along the gate voltage axis. Figure 4-7 shows the experimental non-steady-state channel conductance vs gate voltage curve for an acid solution. The hysteresis results from the fact that the devices, because of slow ambipolar diffusion, are not in steady state. This can be compared with the theoretical non-steady-state conductance curve in Figure 4-6, which predicts the hysteresis for an acid solution.

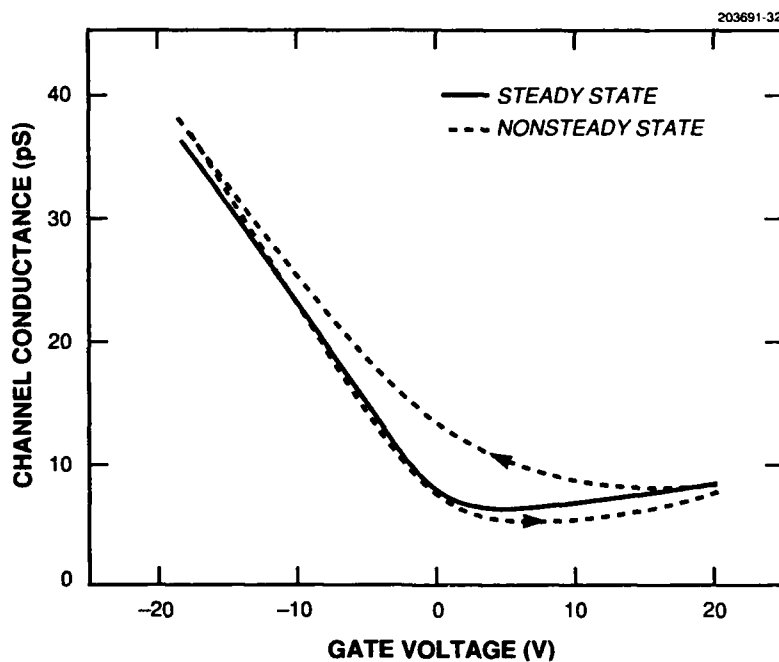


Figure 4-6. Theoretical steady-state and non-steady-state channel conductance vs gate voltage curves for a channel filled with 5×10^{-4} -M acid in glycerol with cation and anion mobility of 7.85×10^{-6} and $1 \times 10^{-6} \text{ cm}^2 \text{ V}^{-1} \text{ s}^{-1}$, respectively. The non-steady-state curve is interpolated from 10-V steps in gate voltage, starting at 20 V and occurring 66.7 min apart, in which the gate capacitance is fully charged but the device has not reached steady state by ambipolar diffusion before the gate voltage is stepped again.

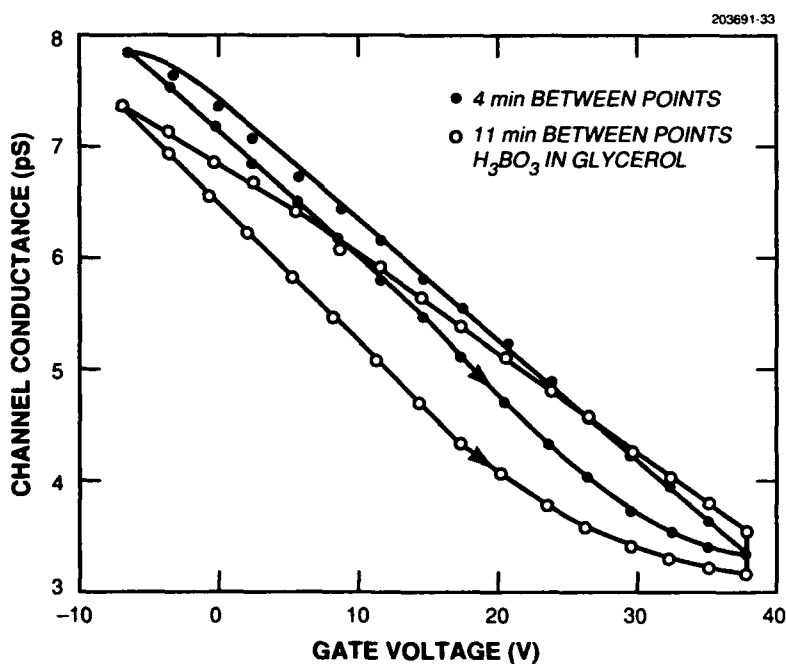


Figure 4-7. Experimental non-steady-state channel conductance vs gate voltage curve for a 1.8×10^{-3} -M glycerol solution of H_3BO_3 . The hysteresis is counterclockwise, as predicted in Figure 4-6.

Our experiments indicated an unexpected positive shift of 20 V in the channel conductance vs gate voltage curves, which could be explained by a fixed negative charge of $1.2 \mu\text{C cm}^{-2}$ on the Si_3N_4 surfaces. Alternatively, differences between experiment and theory may be due to ions binding to the surface. Some of the channel conductance transient response curves had inflections, which would not be present if just ambipolar diffusion were acting. For purposes of developing the chemical analyzers, the most important concept experimentally verified by the ILCFET was the ability of the gate voltage to control the channel ion concentrations.

S. A. Gajar
M. W. Geis

REFERENCES

1. Solid State Research Report, Lincoln Laboratory, MIT, 1990:4, p. 51.
2. W. N. Partlo and W. G. Oldham, *Proc. SPIE* **1264**, 564 (1990).
3. W. Buck, private communication.
4. S. A. Gajar, Ph.D. thesis, Massachusetts Institute of Technology, 1992.
5. O. F. Devereux and P. L. deBruyn, *Interaction of Plane-Parallel Double Layers* (M.I.T. Press, Cambridge, Mass., 1963).

5. HIGH SPEED ELECTRONICS

5.1 DEFINITIVE IDENTIFICATION OF D^- CENTERS IN GaAs QUANTUM WELLS BY TILT-INDUCED LINE SPLITTING IN A MAGNETIC FIELD

D^- centers, two-electron ions formed by attaching a second electron to a shallow hydrogenic donor (D^0), have proven more difficult to detect than the shallow donor centers themselves. Isolated D^- centers were found in bulk GaAs only in those rare n -type epitaxial samples that were simultaneously of high purity and very low compensation [1]. Identification of this center in GaAs was first achieved by comparing theoretical predictions of its photoionization energy [2] with measured values as a function of magnetic field.

Although shallow donors have been clearly identified in center-doped GaAs/AlGaAs quantum wells by far-infrared (FIR) magnetospectroscopy [3], the D^- center has proven more elusive. It is to be expected that donor-doped GaAs quantum wells enclosed by n -type AlGaAs barriers should be rich in electrons, a condition favoring D^- formation. So far, however, no definitive evidence for such centers has been adduced. This, it appears, is due partly to a fundamentally incorrect understanding of the nature of the final states reached in D^- optical transitions, partly to a lack of relevant theoretical calculations, and partly to the fact that the D^- transition energies in a limited range of magnetic field can coincide, more or less, with those of donors located at a selected position in the well between the center and the barrier edge. It is necessary to rule out the possibility that an observed line belongs to a donor before it can be assigned with certainty to the D^- center.

The experimental setup and sample employed in the present work are described in detail in [4]. Briefly, the spectral data are obtained by monitoring, as a function of swept magnetic field, the in-plane photoconductivity of a center-doped GaAs/AlGaAs quantum-well sample (with no intentional barrier doping) illuminated by FIR laser radiation. Data with a high signal-to-noise ratio are obtained.

In the present work the relative positions of three D^- levels are identified in the FIR spectrum of 51-nm GaAs quantum wells. First, the separation of the ground-state level and the lowest excited $M = +1$ level is studied, as in previous work, at $\theta = 0^\circ$, where θ is the angle between the magnetic field and the z direction. In this configuration, agreement between the calculated and observed transition energies is found to be within 1 cm^{-1} . Second, an anticrossing is induced between the lowest excited $M = +1$ level and the lowest level of odd z parity by tilting the sample. (Wave functions that are odd functions of z are defined to have odd z parity.) In the present study the data were taken at $\theta = 16^\circ$ and 31° . Typical data at these angles are shown in Figure 5-1. Good agreement is found between these measurements and the theory for D^- levels, as shown in Figure 5-2. The agreement is obtained, moreover, without the use of any adjustable parameters.

Attempts were made to see if a location in the well could be found theoretically where a neutral donor would have a $1s \rightarrow 2p_{+1}$ behavior that replicates the data shown in Figure 5-2(a) and displays anticrossings comparable to those in Figures 5-2(b) and 5-2(c). The infinite barrier model ($V_0 = \infty$) was employed with the donor-excited-state calculation of [5], modified to be applicable to donors away from the well center; this gives a best fit to the data of Figure 5-2(a) for a hypothetical spike in the

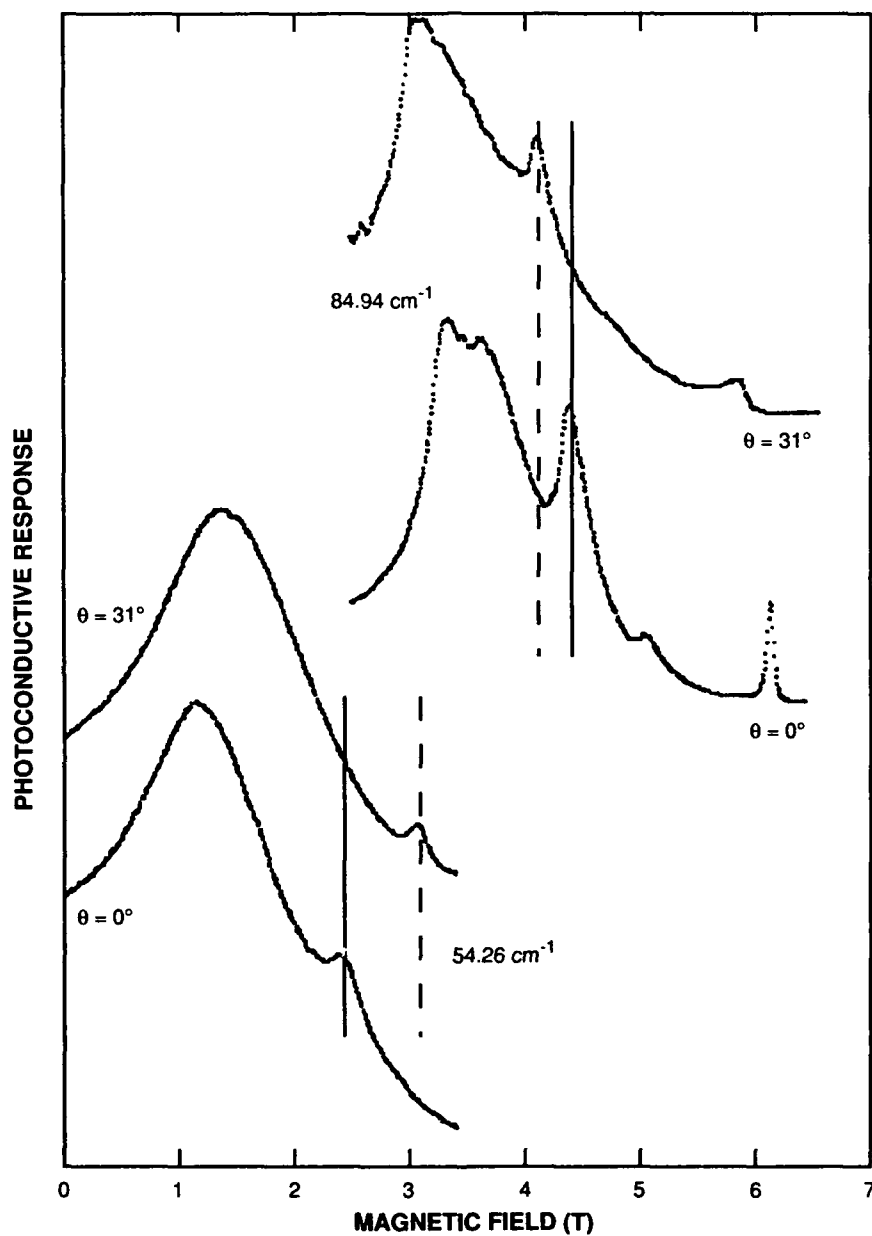


Figure 5-1. Photoconductivity data above (84.94 cm^{-1}) and below (54.26 cm^{-1}) the D^- level crossing for $\theta = 0^\circ$ and 31° . Vertical lines (dashed for $\theta = 31^\circ$ and solid for $\theta = 0^\circ$) locate the D^- peaks. The strong lower-field peaks are from the donor $1s \rightarrow 2p_{x1}$ transition.

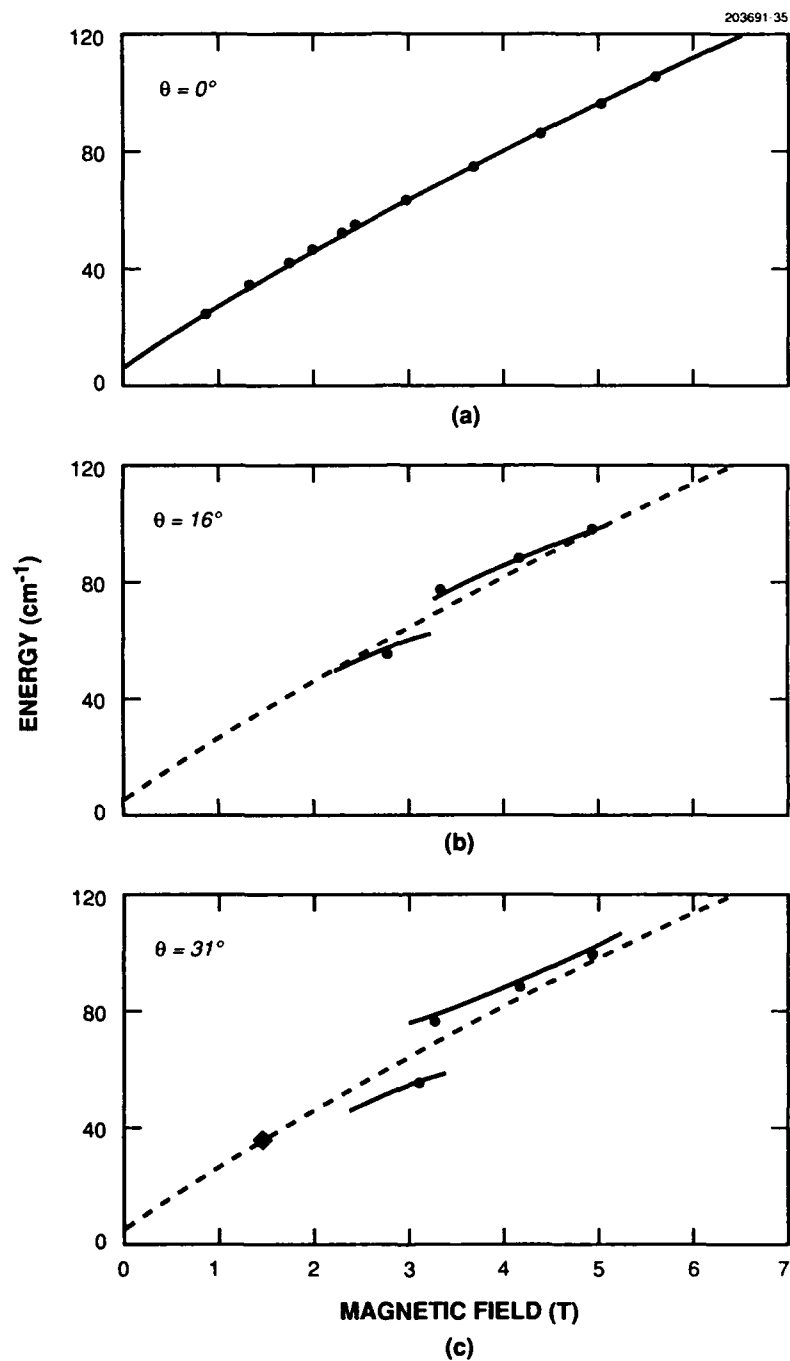


Figure 5-2. Transition energy vs magnetic field for line b of [4]. The magnetic field in (a) to (c) makes an angle $\theta = 0^\circ$, 16° , and 31° , respectively, relative to the normal to the well planes. The dots represent data and the solid lines represent theory. The diamond is a data point for $\theta = 26^\circ$. The dashed lines in (b) and (c) display the theoretical results for $\theta = 0^\circ$.

concentration of donors located ~ 19 nm from the center of the well. The best $1s \rightarrow 2p_{+1}$ transition curve that was found deviates from the data by as much as $\pm 4 \text{ cm}^{-1}$ and is concave upward rather than concave downward like the data. At $\theta = 0^\circ$, the nearest level to which the $2p_{+1}$ donor level could couple by tilting the sample is more than 4 cm^{-1} away from the $2p_{+1}$ level at fields near those observed for level crossings. Thus, no behavior resembling Figures 5-2(b) and 5-2(c) could be obtained from the donor transition model.

E. R. Mueller*	J. Waldman*
D. M. Larsen*	W. D. Goodhue

REFERENCES

1. C. J. Armistead, S. P. Najda, P. A. Makado, R. A. Stradling, P. C. Coulter, and G. E. Stillman, *Solid State Commun.* **48**, 51 (1983); C. J. Armistead, S. P. Najda, R. A. Stradling, and J. C. Maan, *Solid State Commun.* **53**, 1109 (1985).
2. D. M. Larsen, *Phys. Rev. B* **20**, 5217 (1979).
3. N. C. Jarosik, B. D. McCombe, B. V. Shanabrook, J. Comas, J. Ralston, and G. Wicks, *Phys. Rev. Lett.* **54**, 1263 (1985).
4. E. R. Mueller, W. D. Goodhue, D. M. Larsen, J. W. Bales, and J. Waldman, *Phys. Rev. B* **44**, 1754 (1991).
5. D. M. Larsen, *Phys. Rev. B* **44**, 5629 (1991).

*Author not at Lincoln Laboratory.

6. MICROELECTRONICS

6.1 DNA SEQUENCE DETECTION USING CHARGE-COUPLED DEVICES

A charge-coupled device (CCD) has been used to detect hybridization of a target DNA sequence to probe DNA sequences. The CCD detects the presence of a radioisotope label attached to a target DNA strand at sites where hybridization between the target and probe has occurred. This work is part of an effort to establish an efficient method for the mapping of the human genome. A large-area, high-resolution CCD to which many probes with different sequences have been attached provides a way to evaluate many trial sequences in a very short time.

The DNA sequence decoding is done by the sequencing-by-hybridization method, i.e., by pairing known synthetic probe sequences to an unknown target sequence and then determining which of the probes have successfully hybridized [1]–[3] with the target. Binding of the probe and target occurs with the greatest affinity at those sites where the probe sequence is exactly complementary to some portion of the target sequence. Table 6-1 gives an example of a target and a set of probes. A 21-mer target is compared to four different 9-mer probes. In this case, probe C is an exact complementary match to a segment of the target G DNA and therefore should have the strongest binding to the target. The other three probes vary only by one base from the target (a base is designated by a single letter as presented in Table 6-1), and therefore this is a stressing test of the discrimination of the technique.

TABLE 6-1
Example of Sequencing by Hybridization*

Strand Label	Sequence
Probe G	3'-ACTAGCGAT-5'
Probe A	3'-ACTAACGAT-5'
Probe C	3'-ACTACCGAT-5'
Probe T	3'-ACTATCGAT-5'
Target G	5'-TCAGGCTGATGGCTAAGTCCA-3'
*Probes G and A are complementary to probes C and T, respectively.	

The pairing of the probe and target DNA to detect hybridization was done directly on the surface of a CCD imager. For this example, probes with the four 9-mer sequences given in Table 6-1 were placed on the CCD in separate quadrants of the 420×420 imaging array and covalently linked to the surface. Each quadrant contained a 3.5-mm-diam dot of the probe DNA as conceptually shown in Figure 6-1. Then, the target DNA containing the radioisotope label ^{32}P was applied to the CCD surface. After

allowing sufficient time for hybridization to occur, the CCD was washed to remove the unhybridized target DNA. Figure 6-1 also shows the expected condition of DNA on the CCD surface after rinsing where the target strands had attached to the shorter probe strands. The radioisotope was covalently bonded at those sites where hybridization had occurred.

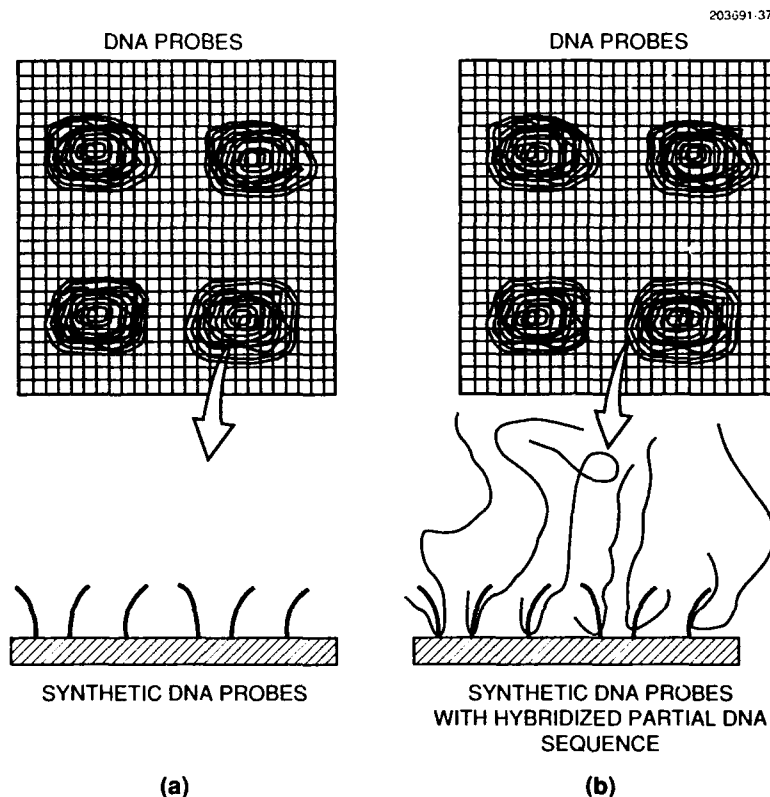


Figure 6-1. Implementation of sequencing by hybridization using a 420×420 imager, showing arrays of DNA probes (a) before and (b) after hybridization.

The beta particle emitted by ^{32}P has an energy of about 1.7 MeV and is sufficient to create several hundred thousand electron-hole pairs in the CCD silicon substrate. Figure 6-2 shows a map of detected photoelectrons vs pixel location in the 420×420 -pixel CCD imaging area. The bright areas in the map indicate locations of collected charge. The four different probe sites are easily distinguished in the map, illustrating that hybridization has occurred at all sites. The lower right-hand quadrant was the only site that contained the exact complementary sequence to a segment of target DNA (probe C) and therefore should have been the most active location, but this location showed the lowest apparent level of radioactivity. In spite of this unexplained reversal of the expected radioactivity of the sites, the lower right-hand site was well differentiated from the others. The relative activity levels of the four dots detected by the CCD was independently confirmed using photographic film. Current work is aimed at repeating the experiment to resolve the inconsistency.

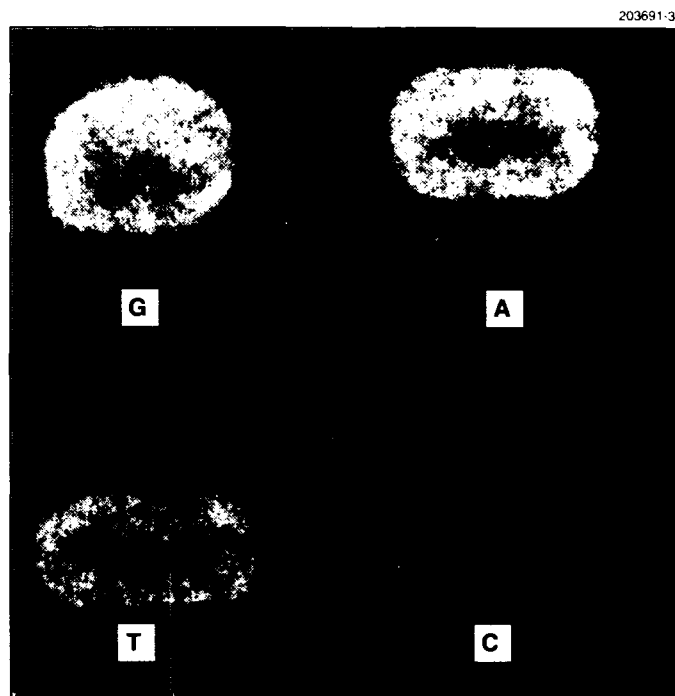


Figure 6-2. Hybridization map generated by a CCD imager.

R. K. Reich	M. E. Hogan*
V. S. Dolat	M. A. Hollis
B. E. Burke	M. D. Eggers*

REFERENCES

1. R. Dmanac, I. Labat, I. Buckner, and R. Crkvenjakov, *Genomics* **4**, 114 (1989).
2. K. R. Khrapko, P. Y. Lysov, A. A. Khorlin, V. V. Shick, V. L. Florentiev, and A. D. Mirzabekov, *FEBS Lett.* **256**, 118 (1989).
3. W. Bains and G. C. Smith, *J. Theor. Biol.* **135**, 303 (1988).

*Author not at Lincoln Laboratory.

7. ANALOG DEVICE TECHNOLOGY

7.1 MULTILAYER 12-GHz MICROSTRIP ANTENNA ARRAY WITH A HIGH- T_c SUPERCONDUCTING FEED NETWORK

High- T_c superconductors have made it possible to fabricate transmission lines with extremely low losses that operate at liquid nitrogen temperature. A particularly promising application is high-frequency antenna arrays, in which a high- T_c superconducting feed network can be used to avoid the serious gain reduction caused by ohmic losses in a normal-metal feed network [1]. The design, fabrication, and testing of a 16-element (4×4) microstrip array with a superconducting feed network has been successfully completed. The 16-element array operates at 12 GHz, and only the lower layer of the multilayer structure must be cooled to 77 K.

As shown in Figure 7-1, the structure consists of three layers, which are from top to bottom a quartz superstrate, a vacuum gap, and a LaAlO_3 substrate. The vacuum gap provides thermal insulation between the cold LaAlO_3 layer (77 K) and the nominally room-temperature quartz layer. The quartz superstrate acts as a cryostat window as well as supporting an upper layer of 2- μm -thick silver proximity-coupled microstrip patches. Thus, the quartz layer must withstand the atmospheric pressure difference created by the vacuum inside the cooling apparatus.

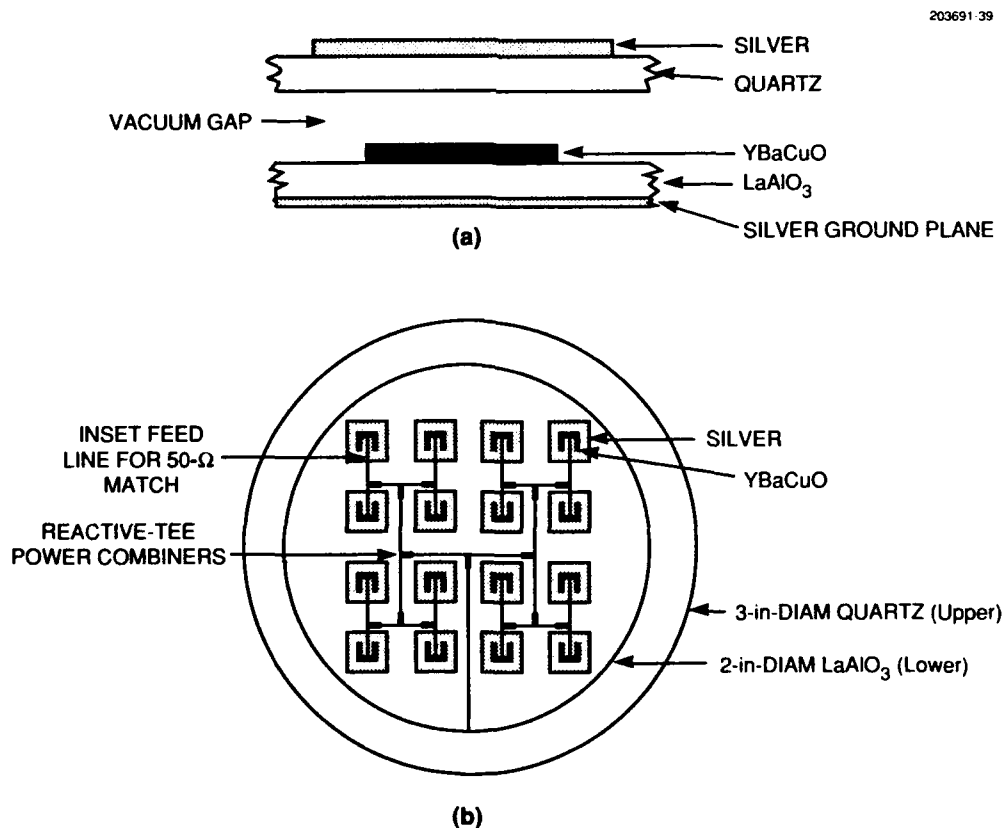


Figure 7-1. (a) Cross section of a single stacked patch in a superconductive microstrip antenna array. (b) Diagram of the structure of the superconductive microstrip stacked-patch antenna array.

A network of power dividers and lower microstrip patches was produced on the LaAlO_3 by patterning a thin film of the high- T_c superconductor $\text{YBa}_2\text{Cu}_3\text{O}_{7-x}$ (YBCO). Standard photoresist processing was used along with a spray etch of 0.25% phosphoric acid to define the feed network pattern in the YBCO [2]. A 2- μm -thick silver ground plane was deposited on the bottom surface of the LaAlO_3 . A silver ohmic contact to the YBCO feed network was defined using liftoff of a photoresist trilayer consisting of AZ 1470, a thin layer of titanium, and poly(methyl methacrylate), and was then annealed at 400°C to establish a mechanically robust contact. Several 75- μm -wide aluminum ribbons were wedge bonded to the ohmic contact and to the microwave connector.

Substrates such as LaAlO_3 with a high dielectric constant create a problem for microstrip arrays. A standard single-layer patch antenna fabricated on LaAlO_3 with a low-temperature dielectric constant of 23.5 would typically have a bandwidth of $\sim 1\%$. The proximity-coupled patches are used because of their broad-bandwidth scanning properties; the arrangement described here can have a bandwidth approaching 10%, even with the lower patches on LaAlO_3 substrates. Since most applications using microstrip arrays require bandwidths of at least several percent, the proximity-coupled patches were a clear choice for development. A multilayer infinite-array dyadic Green's function was used along with the method of moments to design the microstrip antennas and feed lines [3]. This approach models all mutual coupling effects, including surface-wave resonances in large, scanning microstrip arrays.

Initially, measurements were made on elements in a cryogenic waveguide simulator, which experimentally replicates an infinite-array environment. This method allowed the electrical characteristics of an individual element to be examined without any external complications such as power dividers or feed structures. As shown in Figure 7-2, the theoretical model accurately predicts the resonant frequency at ~ 12 GHz, with a measured 2:1 voltage standing-wave ratio (VSWR) bandwidth of 8%.

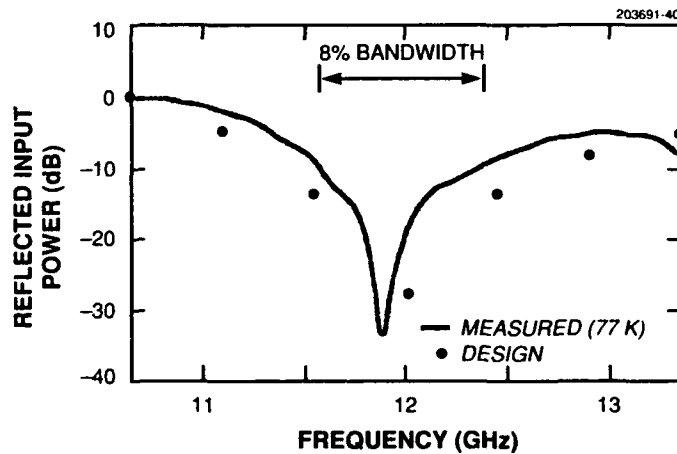


Figure 7-2. Input reflection coefficient vs frequency for superconducting YBCO elements in a cryogenic infinite-array waveguide simulator. Bandwidth is measured using a 2:1 VSWR criterion.

After successful tests of the elements in the waveguide simulator, the 16-element (4×4) array was designed and fabricated with the lower-layer microstrip patches and feed network made from thin-film superconducting YBCO. A photograph of the disassembled array is shown in Figure 7-3. Figure 7-4 shows measured far-field radiation patterns. Both patterns are highly symmetrical about broadside, as

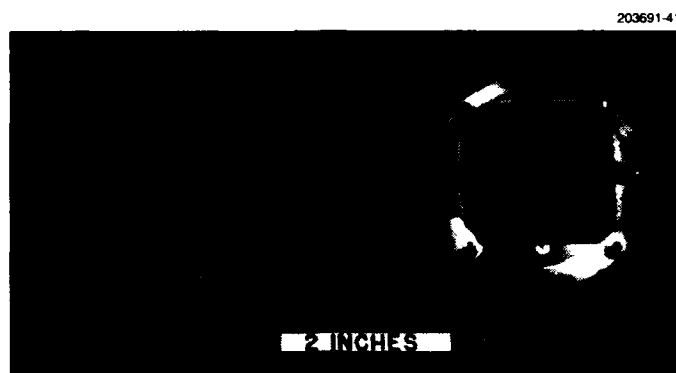


Figure 7-3. Silver upper radiator array (left) and YBCO lower feed array (right) of disassembled superconducting microstrip antenna array.

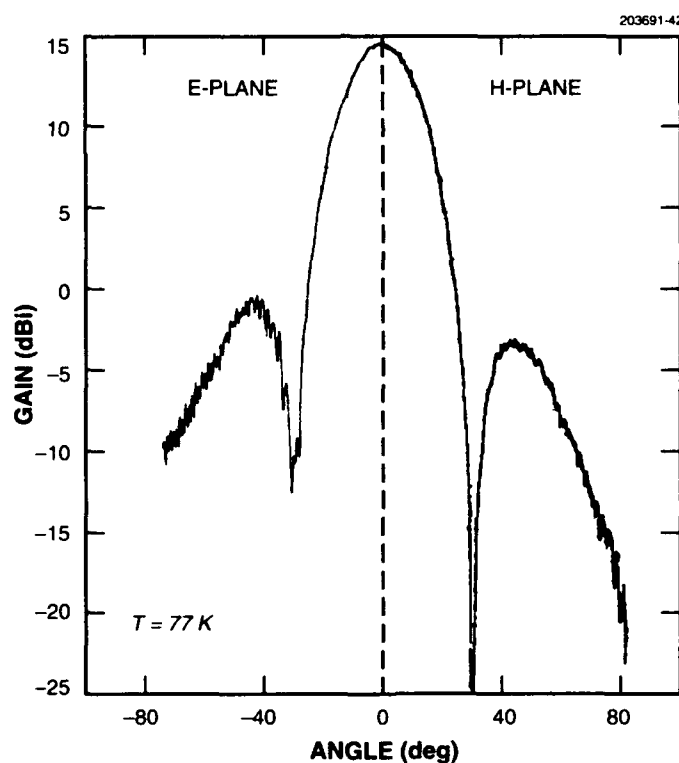


Figure 7-4. Far-field radiation patterns of the superconducting YBCO microstrip array at 12 GHz. Both E- and H-plane patterns were sufficiently symmetric that only half of each is shown on the left- and right-hand sides of the figure, respectively.

expected, since all elements were driven in phase to produce a main beam at broadside. Gain of ~ 15 dBi (compared to isotropic) was measured by calibrating with a standard gain horn. These measurements agreed with the calculated gain of 15.1 dBi.

Measurements have also been made on an array with a fixed main beam pointing 45° from broadside in the E -plane. This array verified the broad-bandwidth properties of the proximity-coupled patch array with the main beam scanned far from broadside. Work is currently under way to develop phase shifters that can be incorporated into the array to provide electronic scanning capability.

W. G. Lyons	J. S. Herd*
A. C. Anderson	K. G. Herd*
P. M. Mankiewich*	M. L. O'Malley*

REFERENCES

1. W. G. Lyons and R. S. Withers, *Microwave J.* **33**(11), 85 (1990).
2. W. G. Lyons, R. S. Withers, J. M. Hamm, A. C. Anderson, P. M. Mankiewich, M. L. O'Malley, R. E. Howard, R. R. Bonetti, A. E. Williams, and N. Newman, *1991 IEEE MTT-S Int. Micro Symp. Dig.* (IEEE, New York, 1991), Vol. 3, p. 1227.
3. J. S. Herd, *1989 Int. Symp. Dig. Antennas and Propagation* (IEEE, New York, 1989), Vol. 2, p. 1150.

*Author not at Lincoln Laboratory.

REPORT DOCUMENTATION PAGE				<i>Form Approved</i> OMB No. 0704-0188	
Public reporting burden for this collection of information is estimated to average 1 hour per response, including the time for reviewing instructions, searching existing data sources, gathering and maintaining the data needed and completing and reviewing the collection of information. Send comments regarding this burden estimate or any other aspect of this collection of information, including suggestions for reducing this burden, to Washington Headquarters Services, Directorate for Information Operations and Reports, 1215 Jefferson Davis Highway, Suite 1204, Arlington, VA 22202-4302, and to the Office of Management and Budget, Paperwork Reduction Project (0704-0188), Washington, DC 20503.					
1. AGENCY USE ONLY (Leave blank)		2. REPORT DATE 15 May 1992		3. REPORT TYPE AND DATES COVERED Quarterly Technical Report, 1 February - 30 April 1992	
4. TITLE AND SUBTITLE Solid State Research				5. FUNDING NUMBERS C — F19628-90-C-0002 PE — 63250F PR — 221	
6. AUTHOR(S) Alan L. McWhorter				8. PERFORMING ORGANIZATION REPORT NUMBER 1992:2	
7. PERFORMING ORGANIZATION NAME(S) AND ADDRESS(ES) Lincoln Laboratory, MIT P.O. Box 73 Lexington, MA 02173-9108					
9. SPONSORING/MONITORING AGENCY NAME(S) AND ADDRESS(ES) HQ Air Force Material Command AFMC/STSC Wright-Patterson AFB, OH 45433-5001				10. SPONSORING/MONITORING AGENCY REPORT NUMBER ESC-TR-92-129	
11. SUPPLEMENTARY NOTES None					
12a. DISTRIBUTION/AVAILABILITY STATEMENT Approved for public release; distribution is unlimited.				12b. DISTRIBUTION CODE	
13. ABSTRACT (Maximum 200 words) <p style="text-align: center;">This report covers in detail the research work of the Solid State Division at Lincoln Laboratory for the period 1 February through 30 April 1992. The topics covered are Electrooptical Devices, Quantum Electronics, Materials Research, Submicrometer Technology, High Speed Electronics, Microelectronics, and Analog Device Technology. Funding is provided primarily by the Air Force, with additional support provided by the Army, DARPA, Navy, SDIO, NASA, and DOE.</p>					
14. SUBJECT TERMS electrooptical devices quantum electronics materials research submicrometer technology		high speed electronics microelectronics analog device technology lasers laser arrays	optical modulators optical interconnects laser microwave generation mass transport epitaxial growth	ultraviolet lithography ionic transistors semiconductor defects DNA sequencing superconductive antenna arrays	15. NUMBER OF PAGES 80
17. SECURITY CLASSIFICATION OF REPORT Unclassified		18. SECURITY CLASSIFICATION OF THIS PAGE SAR	19. SECURITY CLASSIFICATION OF ABSTRACT SAR		16. PRICE CODE
20. LIMITATION OF ABSTRACT SAR					